

AN ATLAS OF [N II] AND [O III] IMAGES AND SPECTRA OF PLANETARY NEBULAE

ARSEN R. HAJIAN,¹ STEVEN M. MOVIT,^{1,2} DENIS TROFIMOV,^{1,3} BRUCE BALICK,⁴ YERVANT TERZIAN,⁵
 KEVIN H. KNUTH,^{6,7} DOMHNALL GRANQUIST-FRASER,⁸ KAREN A. HUYSER,⁹ ANDRE JALOBÉANU,¹⁰
 DAWN MCINTOSH,⁶ ANNE E. JASKOT,^{1,11} STACY PALEN,^{12,13} AND NINO PANAGIA^{14,15}

Received 2004 June 30; accepted 2006 November 26

ABSTRACT

We present an atlas of *Hubble Space Telescope* images and ground-based, long-slit, narrowband spectra centered on the 6584 Å line of [N II] and the 5007 Å line of [O III]. The spectra were obtained for a variety of slit positions across each target (as shown on the images) in an effort to account for nonspherical nebular geometries in a robust manner. We have extended the prolate ellipsoidal shell model originally devised by Aaquist, Zhang, and Kwok to generate synthetic images, *as well as* long-slit spectra. Using this model, we have derived basic parameters for the subsample of PNe that present ellipsoidal appearances and regular kinematic patterns. We find differences between our parameters for the target PNe as compared to those of previous studies, which we attribute to increased spatial resolution for our image data and the inclusion of kinematic data in the model fits. The data and analysis presented in this paper can be combined with detections of nebular angular expansion rates to determine precise distances to the PN targets.

Subject headings: atlases — planetary nebulae: general

1. INTRODUCTION

Planetary nebula (PN) distances are commonly determined via indirect methods. A physical quantity is assumed to be common to and constant for all PNe, yielding fractional distance uncertainties of >150%, and distances suitable only for statistical surveys. Despite the surprisingly precise ground-based results from astrometric telescopes and careful calibration (Harris et al. 1997), only about a dozen PNe yield accurate results.

Without accurate distances to the vast majority of individual PNe, some of the most important astrophysical properties of PNe remain obscure despite many decades of observations. Among these are mass and luminosity; estimators for both are strongly distance dependent, and they are important for several critical projects including stellar evolution and mass loss, the PN lumi-

nosity function, galactic dynamics and energy balance, and the cosmological distance scale.

We have started a program of individual distance measurements to a collection of PNe using the expansion parallax method (Masson 1986; Palen et al. 2002). Our strategy (Hajian et al. 1993; Reed et al. 1999) is to measure the angular expansion rate of PNe by comparing at least two epochs of image data obtained with a time separation of several years between epochs. The expansion velocity of the PN is determined using nebular spectroscopy and a spatiokinematic model of the nebula. The resulting distance is therefore just the quotient of the kinematic expansion rate and the angular expansion rate.

Our immediate goal is to obtain high-dispersion, narrowband, long-slit spectra of target PNe with the slit oriented generally along the nebular major and/or minor axis. Multiple slit positions were obtained in order to more precisely determine the nebular kinematic geometry. We also have extended the prolate ellipsoidal shell model by Aaquist & Kwok (1996) and Zhang & Kwok (1998) to generate synthetic long-slit spectra in addition to synthetic images of the target PNe. We use this model to determine geometric parameters (notably the inclination of the major axis to the line of sight) for the nebulae so that precise expansion distances can be computed and systematic distance errors can be significantly reduced. We present our collection of spatiokinematic data and the modeling results in this paper as an archive for future PN studies. We intend to follow this work with a paper in the *Astrophysical Journal* reporting the nebular expansion distances and resulting astrophysical implications.

2. DESCRIPTION OF THE SOURCES AND OBSERVATIONS

2.1. Images

During *Hubble Space Telescope* (HST) Observing Cycles 7, 8, and 9, we obtained numerous images of PNe with the WFPC2 camera using the F502N filter to isolate light from the [O III] line and the F658N filter for the [N II] line. The images were reduced using the standard STSDAS tasks in IRAF. The multiple exposures for each filter/target were processed to remove cosmic rays

¹ Department of Astrometry, US Naval Observatory, Washington, DC 20392-5420.

² Current address: Department of Astronomy and Astrophysics, Pennsylvania State University, University Park, PA 16802.

³ Current address: Orbital Sciences Corporation, Space Systems Group, Dulles, VA 20166.

⁴ Department of Astronomy, University of Washington, Seattle, WA 98195-1580.

⁵ Department of Astronomy and National Astronomy and Ionosphere Center, Cornell University, Ithaca, NY 14853-6801.

⁶ Intelligent Systems Division, NASA Ames Research Center, Moffett Field, CA 94035.

⁷ Current address: Department of Physics, University of Albany, State University of New York, Albany, NY 12222.

⁸ QSS Group, Inc., NASA Ames Research Center, Moffett Field, CA 94035.

⁹ Education Association, NASA Ames Research Center, Moffett Field, CA 94035.

¹⁰ LSIIT (UMR 7005 CNRS-ULP) at Ecole Nationale Supérieure de Physique de Strasbourg, Illkirch, France.

¹¹ Department of Astronomy, Williams College, Williamstown, MA 01267.

¹² Department of Astronomy, University of Washington, Seattle, WA 98195-1580.

¹³ Current address: Physics Department, Weber State University, Ogden, UT 84408.

¹⁴ Space Telescope Science Institute, Baltimore, MD 21218.

¹⁵ On assignment from the Space Telescope Operations Division, Research and Scientific Support Department of ESA.

Report Documentation Page				Form Approved OMB No. 0704-0188	
Public reporting burden for the collection of information is estimated to average 1 hour per response, including the time for reviewing instructions, searching existing data sources, gathering and maintaining the data needed, and completing and reviewing the collection of information. Send comments regarding this burden estimate or any other aspect of this collection of information, including suggestions for reducing this burden, to Washington Headquarters Services, Directorate for Information Operations and Reports, 1215 Jefferson Davis Highway, Suite 1204, Arlington VA 22202-4302. Respondents should be aware that notwithstanding any other provision of law, no person shall be subject to a penalty for failing to comply with a collection of information if it does not display a currently valid OMB control number.					
1. REPORT DATE APR 2007		2. REPORT TYPE N/A		3. DATES COVERED -	
4. TITLE AND SUBTITLE An Atlas of [N ii] and [O iii] Images and Spectra of Planetary Nebulae				5a. CONTRACT NUMBER	
				5b. GRANT NUMBER	
				5c. PROGRAM ELEMENT NUMBER	
6. AUTHOR(S)				5d. PROJECT NUMBER	
				5e. TASK NUMBER	
				5f. WORK UNIT NUMBER	
7. PERFORMING ORGANIZATION NAME(S) AND ADDRESS(ES) US Naval Observatory Department of Astrometry Washington, DC 20392-5420				8. PERFORMING ORGANIZATION REPORT NUMBER	
9. SPONSORING/MONITORING AGENCY NAME(S) AND ADDRESS(ES)				10. SPONSOR/MONITOR'S ACRONYM(S)	
				11. SPONSOR/MONITOR'S REPORT NUMBER(S)	
12. DISTRIBUTION/AVAILABILITY STATEMENT Approved for public release, distribution unlimited					
13. SUPPLEMENTARY NOTES					
14. ABSTRACT					
15. SUBJECT TERMS					
16. SECURITY CLASSIFICATION OF:			17. LIMITATION OF ABSTRACT SAR	18. NUMBER OF PAGES 39	19a. NAME OF RESPONSIBLE PERSON
a. REPORT unclassified	b. ABSTRACT unclassified	c. THIS PAGE unclassified			

TABLE 1
A SUMMARY OF THE IMAGING OBSERVATIONS

PN (1)	[N II]		[O III]	
	T_{int} (s) (2)	GO/Data Set (3)	T_{int} (s) (4)	GO/Data Set (5)
BD +30 –3639	300	8390/u5hc1203r	600	8390/u5hc1201r
	300	8390/u5hc1204r	300	8390/u5hc1202r
IC 2448	350	8390/u5hc1405r	180	8390/u5hc1403r
	350	8390/u5hc1406r	180	8390/u5hc1404r
	350	8390/u5hc1407r
IC 3568	120	8390/u5hc1508r	600	8390/u5hc1503r
	120	8390/u5hc1509r	600	8390/u5hc1504r
	120	8390/u5hc150ar	600	8390/u5hc1505r
	230	8390/u5hc150br	600	8390/u5hc1506r
	230	8390/u5hc150cr	600	8390/u5hc1507r
IC 418	200	8773/u66b1004m	200	8773/u66b1001m
	200	8773/u66b1005m	200	8773/u66b1002m
	300	8773/u66b1006m	200	8773/u66b1003m
IC 4663	700	8773/u66b1203m	400	8773/u66b1201m
	700	8773/u66b1204m	400	8773/u66b1202m
NGC 3132	350	8390/u5hc0103r	400	8390/u5hc0101r
	350	8390/u5hc0104r	400	8390/u5hc0102r
NGC 5882	300	8390/u5hc0305r	860	8390/u5hc0304r
	300	8390/u5hc0306r
	300	8390/u5hc0307r
	300	8390/u5hc0308r
NGC 5979	600	8390/u5hc0405r	230	8390/u5hc0403r
	600	8390/u5hc0406r	230	8390/u5hc0404r
NGC 6565	400	8773/u66b0104r	260	8773/u66b0101r
	400	8773/u66b0105m	260	8773/u66b0102r
	400	8773/u66b0106r	200	8773/u66b0103r
NGC 6578	400	8390/u5hc0605r	230	8390/u5hc0603r
	400	8390/u5hc0606r	230	8390/u5hc0604r
NGC 6741	300	8773/u66b0404r	300	8773/u66b0401r
	260	8773/u66b0405r	300	8773/u66b0402r
	400	8773/u66b0406r	200	8773/u66b0403r
NGC 6818	500	8773/u66b0204r	160	8773/u66b0201r
	500	8773/u66b0205r	160	8773/u66b0202r
	300	8773/u66b0206r	200	8773/u66b0203r
NGC 6826	400	8390/u5hc0702r
	400	8390/u5hc0703r
	400	8390/u5hc0704r
	400	8390/u5hc0705r
NGC 6884	400	8390/u5hc0805r	260	8390/u5hc0803r
	400	8390/u5hc0806r	300	8390/u5hc0804r
NGC 6886	200	8773/u66b0604r	200	8773/u66b0601r
	200	8773/u66b0605r	200	8773/u66b0602r
	300	8773/u66b0606r	200	8773/u66b0603r
NGC 6891	60	8390/u5hc0907r	60	8390/u5hc0902r
	180	8390/u5hc0908r	60	8390/u5hc0904r
	200	8390/u5hc0909r	120	8390/u5hc0905r
	200	8390/u5hc090ar	120	8390/u5hc0906m
NGC 7026	400	8773/u66b0704r	200	8773/u66b0701r
	400	8773/u66b0705r	160	8773/u66b0702r
	300	8773/u66b0706r	160	8773/u66b0703r
NGC 7354			400	8773/u66b0801r
			300	8773/u66b0802r

NOTE.—All of the data shown in this paper were acquired from projects GO 8390 and GO 8773 (PI: Hajian).

TABLE 2
A SUMMARY OF THE SPECTROSCOPIC OBSERVATIONS

PN (1)	OBS./YEAR (2)	SLITS/ T_{int} (s)	
		[N II] (3)	[O III] (4)
BD +30 –3639	K99	2/15	4/60
IC 2448	C99	...	6/3 × 30
IC 3568	K99	1/3 × 240, 1/120	4/120
IC 418	C99	7/20	7/3 × 20
IC 4663	C99	2/120	...
NGC 3132	C99	4/60	5/3 × 240
NGC 5882	C99	12/60	4/60, 2/3 × 10, 1/10
NGC 5979	C99	...	6/60
NGC 6565	C99	8/60	6/60
NGC 6578	C99	...	9/4 × 30, 1/3 × 120, 4/30
	C00	3/300	...
NGC 6741	C99	2/30	6/30
NGC 6818	C99	10/120	...
NGC 6826	K99	11/120	...
NGC 6884	K99	2/120	4/60
NGC 6886	K99	4/60	4/60
NGC 6891	K99	6/120	...
NGC 7026	K99	17/various	12/various
NGC 7354	K99	...	1/120, 5/18

NOTE.—K99 = KPNO 1999, K00 = KPNO 2000, C99 = CTIO 1999, and C00 = CTIO 2000.

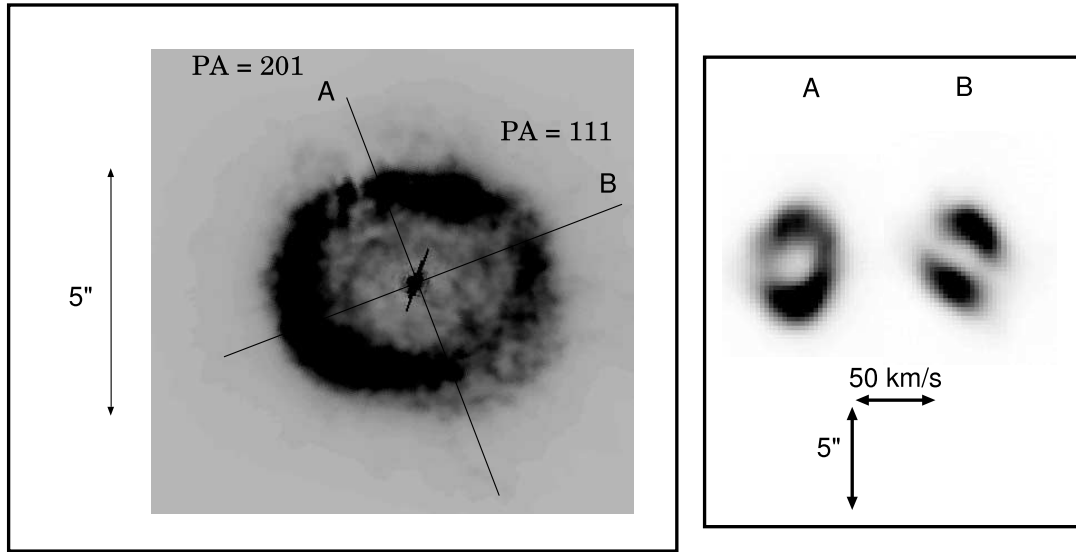
using the IRAF task *crrej*, and the distortion correction was implemented using *drizzle* (Fruchter & Hook 2002) and the Trauger coefficients (Holtzman et al. 1995). Leakage of the $H\alpha$ line into the sharp edges of the F658N bandpass is unavoidable due to the 4%–5% transmission of the filter at 656.3 nm. Correcting for this effect is virtually impossible for this study, since even the Doppler shifts of the $H\alpha$ gas can locally change the transmission through the F658N filter. However, since the $H\alpha$ and [N II] morphologies are usually drastically different in a particular PN (especially for high-ionization PNe), the effects of $H\alpha$ leakage do not affect the analysis in this paper.

A summary of the image observing parameters and sources is shown in Table 1. Column (1) denotes the nebula, and columns (2)–(5) show the integration times and references for the [N II] and [O III] images, respectively. For all but one of the PNe, the image used corresponds to the *HST* WFPC2 image of the PN in the light of the emission line corresponding to the long-slit spectra. The *HST* data sets that were used in constructing the images shown in the paper are tabulated in Table 2. All of the images in this compilation were obtained by us as part of *HST* GO 8773 and 8390 (these images were duplicated in GO 7501). In all of the figures, north is toward the top of the page and east toward the left-hand side.

2.2. Spectroscopy

Echelle data from a target list of PNe were obtained using the 4 m telescopes at the Kitt Peak National Observatory (KPNO) and the Cerro Tololo Inter-American Observatory (CTIO). The KPNO observations were conducted on the nights of 1999 June 25–28 and 2000 April 18–19, and the CTIO observations were conducted on the nights of 1999 May 28–29 and 2000 June 17 and 20.

The spectroscopic observations were obtained in the light of [N II] (6584 Å) and [O III] (5007 Å) whenever possible for three

FIG. 1.— BD +30 -3639 [N II] images from *HST* and spectra from KPNO 1999.

of the four observing runs. For the run at CTIO during 2000, inclement weather permitted only the acquisition of [N II] data. Seeing was variable throughout the observations on timescales of a few hours and generally averaged between $1.0''$ and $1.5''$. The atmospheric conditions were not crucial to the observations due to the narrow observing bandpass, the large aperture, and the generally high surface brightness of the target nebulae. For all four observing runs, the $80''$ decker and $1.5''$ slit were used, and the echelle cross-disperser was replaced with a mirror, so that only one order was obtained centered near the wavelengths of interest. The long-slit capability of the spectrometer required the use of an order-separation filter. To maximize the observations, either [N II] or [O III] data were obtained so as to avoid switching the grating and recalibrating the instrument during the evening. The filters had total bandwidths of $\approx 45 \text{ \AA}$ for the [N II] observations and 80 \AA for the [O III] observations. The instrumental dispersion for the [N II] observations was 0.081 , 0.083 , 0.082 , and $0.081 \text{ \AA pixel}^{-1}$ for the KPNO 1999, KPNO 2000, CTIO 1999, and CTIO 2000 data sets, respectively, corresponding to $\approx 3.7 \text{ km s}^{-1}$. For the

[O III] observations, the instrument dispersion was 0.062 , 0.062 , and $0.060 \text{ \AA pixel}^{-1}$ for the KPNO 1999, KPNO 2000, and CTIO 1999 data sets, respectively, also corresponding to $\approx 3.7 \text{ km s}^{-1}$. By carefully examining unresolved features, we estimate that the spectral resolution of the observations ranges between 1.8 and 2.3 pixels. We expect that systematic errors inherent to the spectrometers and the wavelength calibration process will limit us to $\approx 1 \text{ km s}^{-1}$ accuracy. In the spatial dimension we applied 2 pixel on-chip binning for both CTIO data sets and the KPNO 1999 data set, resulting in $0.50''$ and $0.42'' \text{ pixel}^{-1}$, respectively. For the KPNO 1999 data set, no binning was applied, and the resulting dispersion is $0.21'' \text{ pixel}^{-1}$. The spectroscopic observations are summarized in Table 2. Column (2) shows the observing run that resulted in the data (C = CTIO and K = KPNO), and columns (3) and (4) show the number of slit positions and corresponding integration times for the [N II] and [O III] images, respectively.

All of the PNe studied in this paper are spatially resolved from the ground. Each PN is spanned by at least five spatial resolution elements, so the finite width of the slit, blurring of the apparent

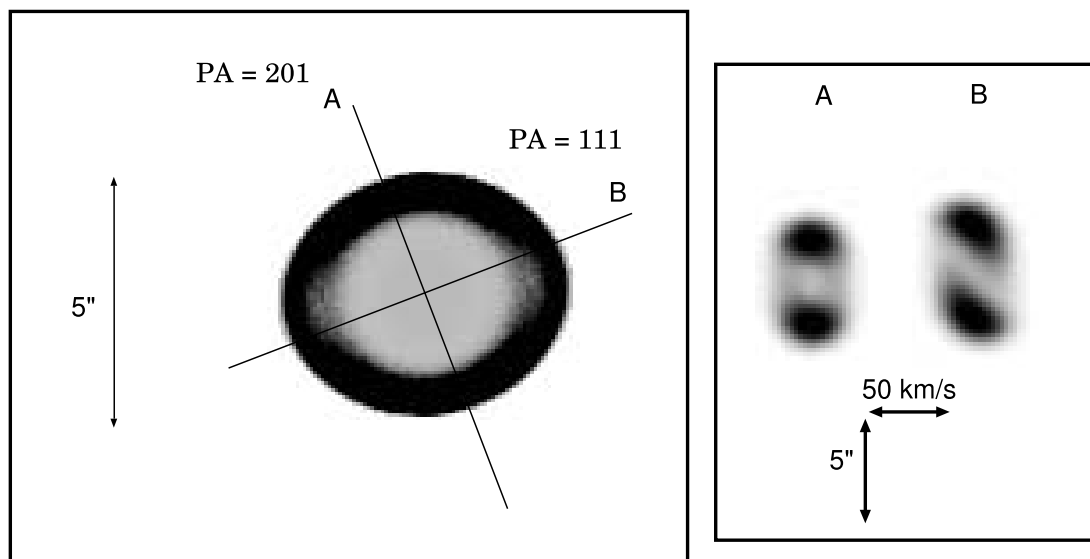


FIG. 2.— BD +30 -3639 [N II] model image and spectra.

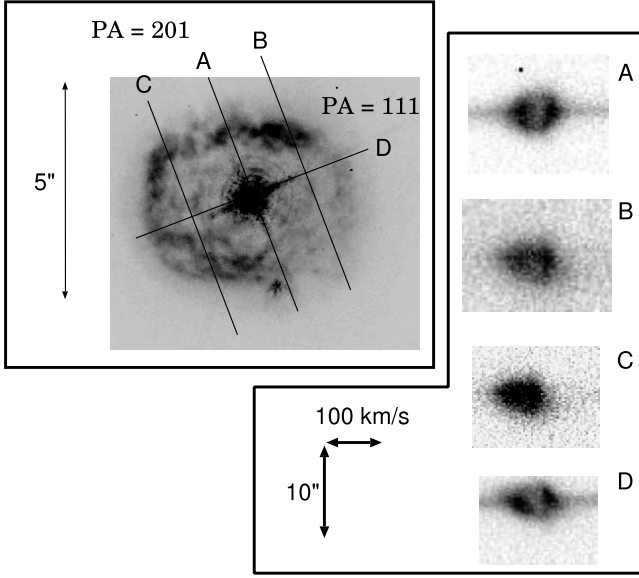


FIG. 3.— BD +30 -3639 [O III] images from *HST* and spectra from KPNO 1999.

slit position on the sky due to seeing, telescope guiding, and differential atmospheric refraction are minimal.

We bias-subtracted the echelle spectra and performed flat-fielding using dome flats. We used thorium-argon lamp spectra to solve for geometric distortions by iteratively executing the IRAF tasks `identify`, `reidentify`, `fitcoords`, and `transform`. In some instances, we used sky lines in the images to test the accuracy of these corrections. There were no significant deviations at the 0.1 pixel level. We also used the lamp spectra to calibrate the wavelength scale. The resulting two-dimensional spectra are shown in Figures 1–56, along with an image of the PN with the slit positions located. In order to determine the slit orientation (i.e., to resolve the 180° ambiguity in the slit position angle), the letters denoting the slit locations on the *HST* images correspond to the end of the slit identified in the spectra.

3. ANALYSIS

3.1. Description of Spatiokinematic Model

The goal of the modeling described below is to infer the spatiokinematic structure of a PN at a particular epoch by fitting models to image and long-slit spectral data. Without this information, large errors can be incurred when radial expansion velocities are married to plane-of-the-sky expansions in order to infer distances. For the subsample of PNe described above, the nebular shells are acceptably approximated by projected, prolate, ellipsoidal shells. We adopt this formalism, which is known as the prolate ellipsoidal shell (PES) model (Aaquist & Kwok 1996; Masson 1989a, 1989b; Zhang & Kwok 1998), and sketch our implementation of the classical model below.

Following the derivation of Aaquist & Kwok (1996, Appendix), we begin with a central star that is a source of ionizing photons and is therefore surrounded by an ionized hydrogen density distribution, $n(\theta, \phi, r)$. We treat this situation similar to that of a Strömgren sphere: the star ionizes the gas to a radius $R_0(\theta, \phi)$ depending on the intervening column density of hydrogen gas (i.e., the nebula is ionization bounded). In addition, we assume that the inner cavity of the PN out to a distance $R_i(\theta, \phi)$ has been vacated by the high-velocity wind from the central star. In addition, we have assumed that all targets are optically thin at the observed wavelengths, which may not be correct in some cases. If we equate the

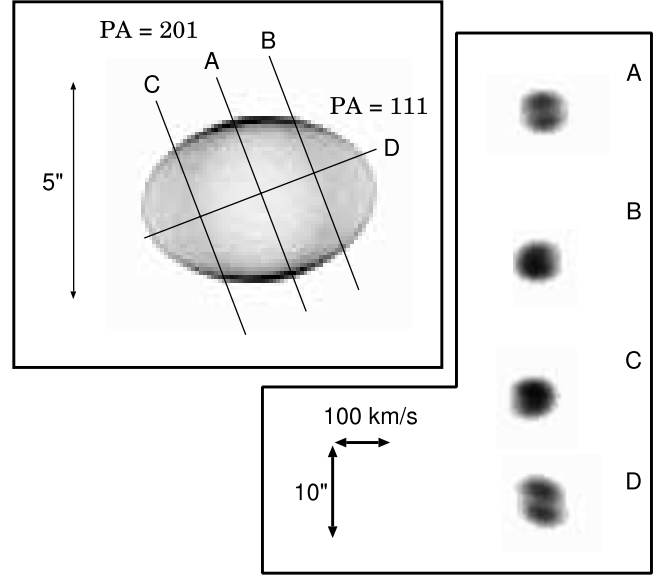


FIG. 4.— BD +30 -3639 [O III] model image and spectra.

number of ionizing photons along a line of sight (left-hand side below) to the number of local recombinations (right-hand side below), we arrive at

$$\frac{dL}{d\Omega} = \int_{R_i}^{R_0} \alpha_B n^2(\theta, \phi, r) r^2 dr, \quad (1)$$

where Ω is the solid angle, L is the stellar ionizing luminosity, and α_B is the hydrogen recombination coefficient (excluding captures to the ground state).

Now we separate the density distribution into three components:

$$n(\theta, \phi, r) = n_0 \eta_\theta(\theta) \eta_\phi(\phi) \eta_r(r), \quad (2)$$

where $n_0 = n(0, 0, R_i)$ [i.e., $\eta_r(r = R_i) = 1$, $\eta_\theta(\theta = 0) = 1$, $\eta_\phi(\phi = 0) = 1$], the angle θ is with respect to the polar axis, and the angle ϕ is the azimuthal coordinate. Note that the model PN is symmetric with respect to the angle ϕ . If we choose a radial power-law distribution of the form

$$\eta_r = \left(\frac{r}{R_i} \right)^{-\gamma}, \quad (3)$$

then equation (1) has an analytic solution of the form

$$\frac{dL}{d\Omega} = \frac{\alpha_B n_0^2 \eta_\theta^2 \eta_\phi^2 R_i^3}{-2\gamma + 3} \left[\left(\frac{R_0}{R_i} \right)^{-2\gamma+3} - 1 \right]. \quad (4)$$

The above model is physically meaningful only if $dL/(d\Omega) > 0$ and if $R_i < R_0$, which can only be satisfied for $\gamma < 1.5$. The azimuthal density distribution is parameterized by

$$\eta_\theta = \begin{cases} (1 - \beta) \left[\left(\frac{2\theta}{\pi} \right)^\alpha + \frac{\beta}{1 - \beta} \right], & \text{for } 0 \leq \theta \leq \frac{\pi}{2}, \\ (1 - \beta) \left[\left(\frac{2\pi - 2\theta}{\pi} \right)^\alpha + \frac{\beta}{1 - \beta} \right], & \text{for } \frac{\pi}{2} \leq \theta \leq \pi, \end{cases} \quad (5)$$

where α is the latitudinal density gradient and β is the ratio of the polar to equatorial density.

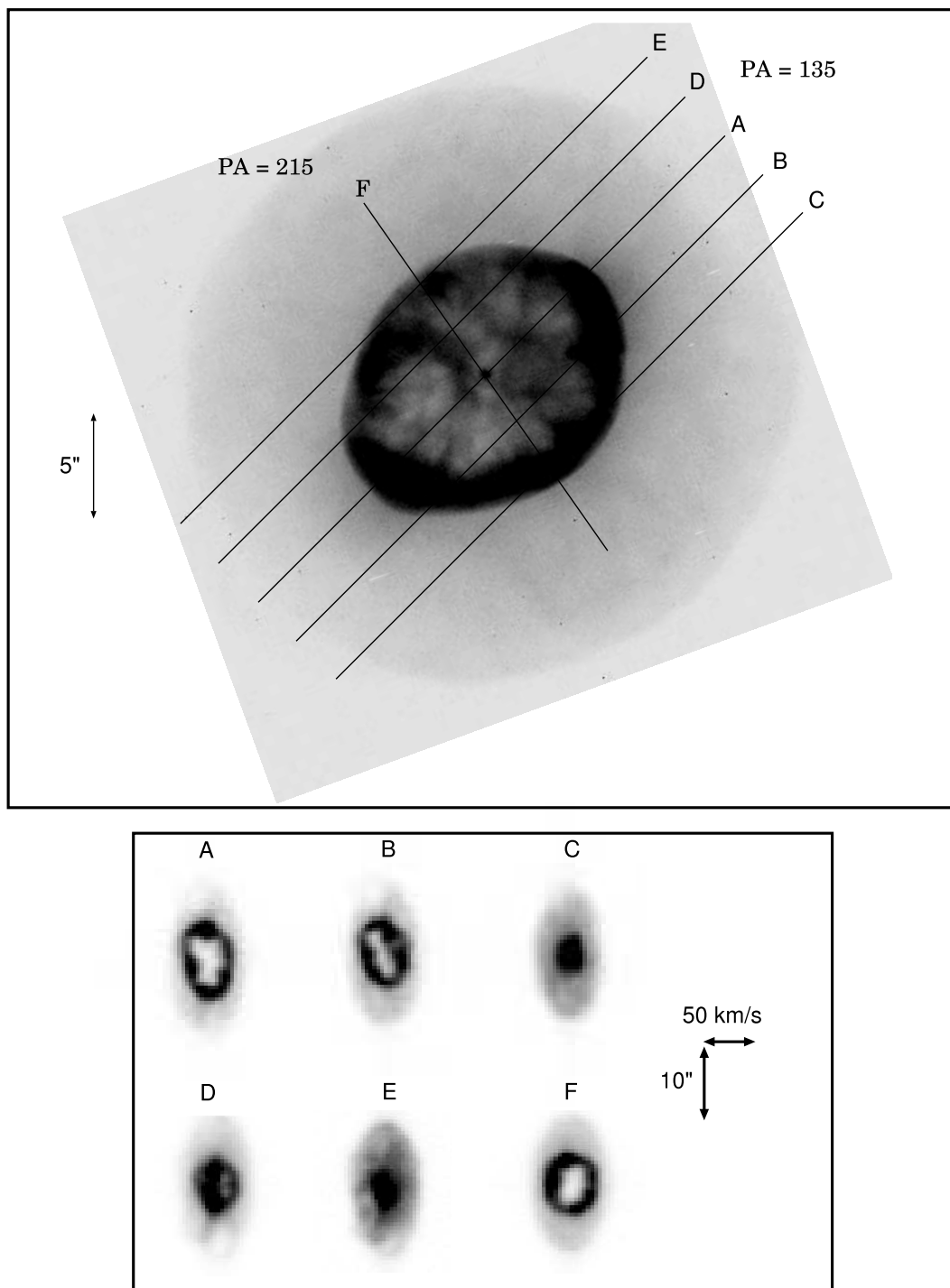


FIG. 5.—IC 2448 [O III] images from *HST* and spectra from CTIO 1999.

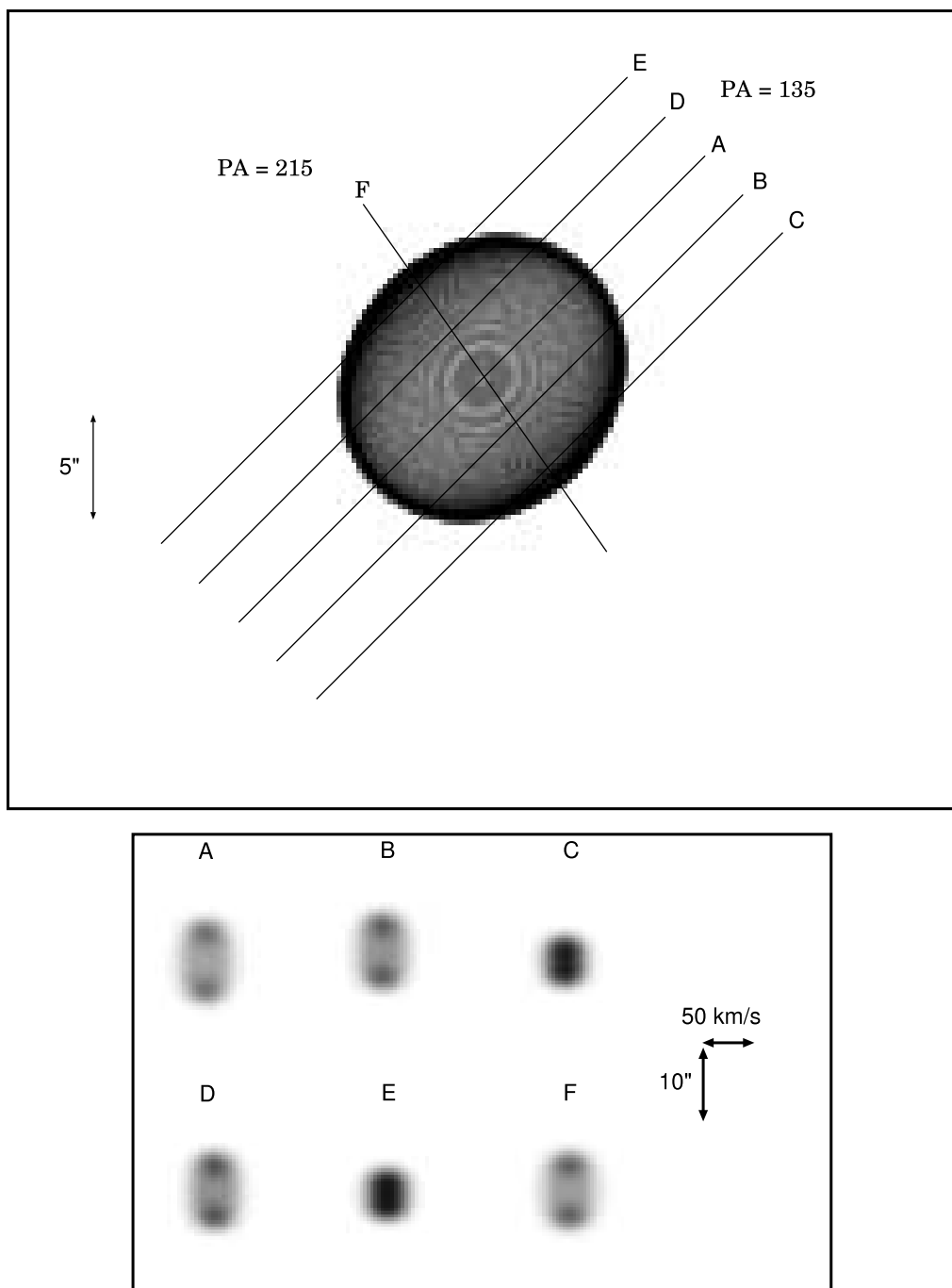


FIG. 6a

FIG. 6.—(a) IC 2448 [O III] core model image and spectra of nebular core. (b) IC 2448 [O III] halo model image and spectra of nebular halo.

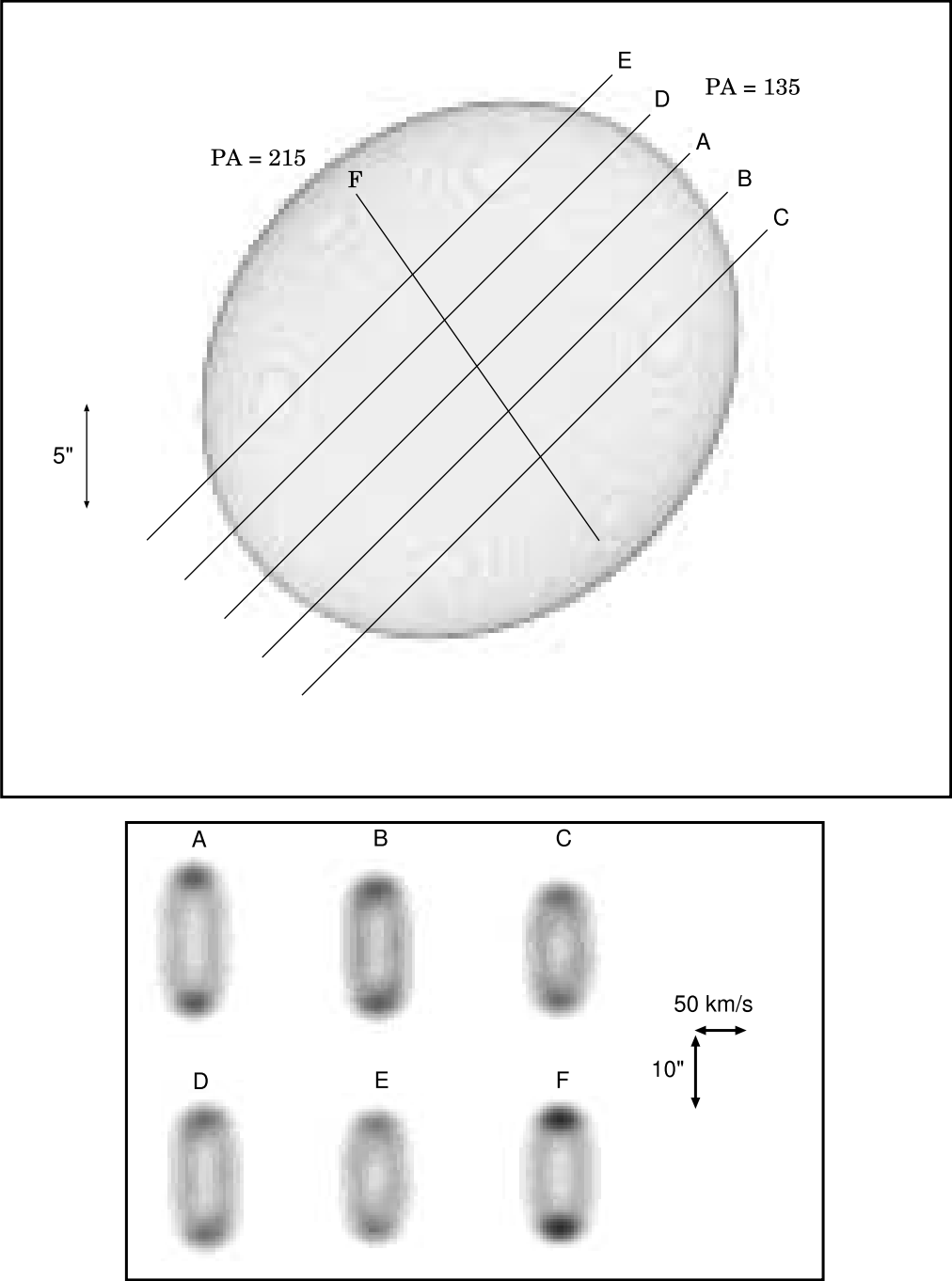


FIG. 6*b*

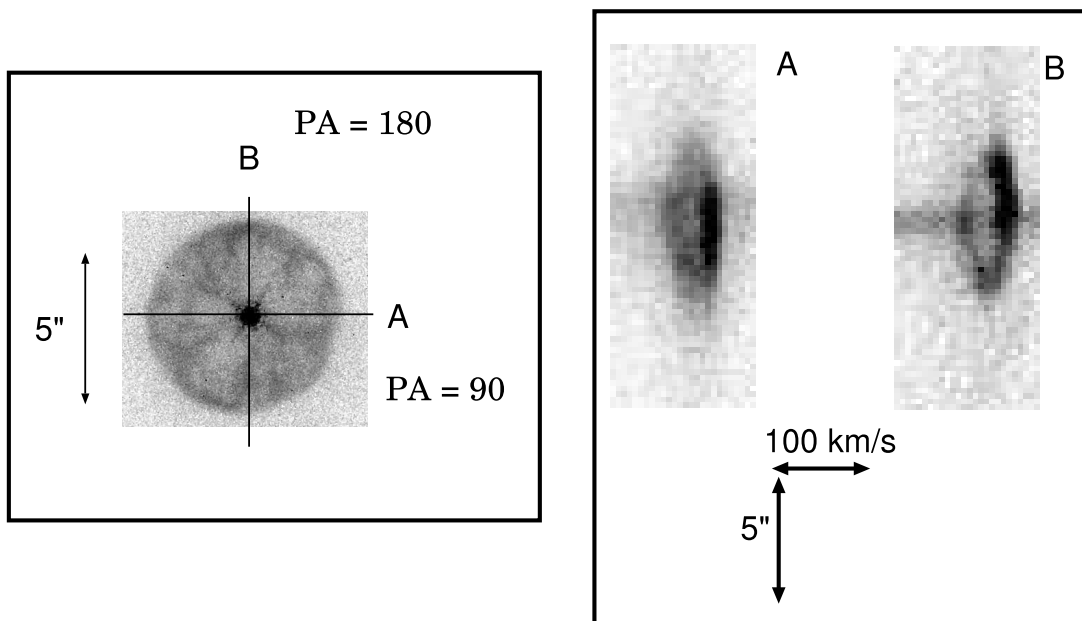


FIG. 7.—IC 3568 [N II] images from *HST* and spectra from KPNO 1999.

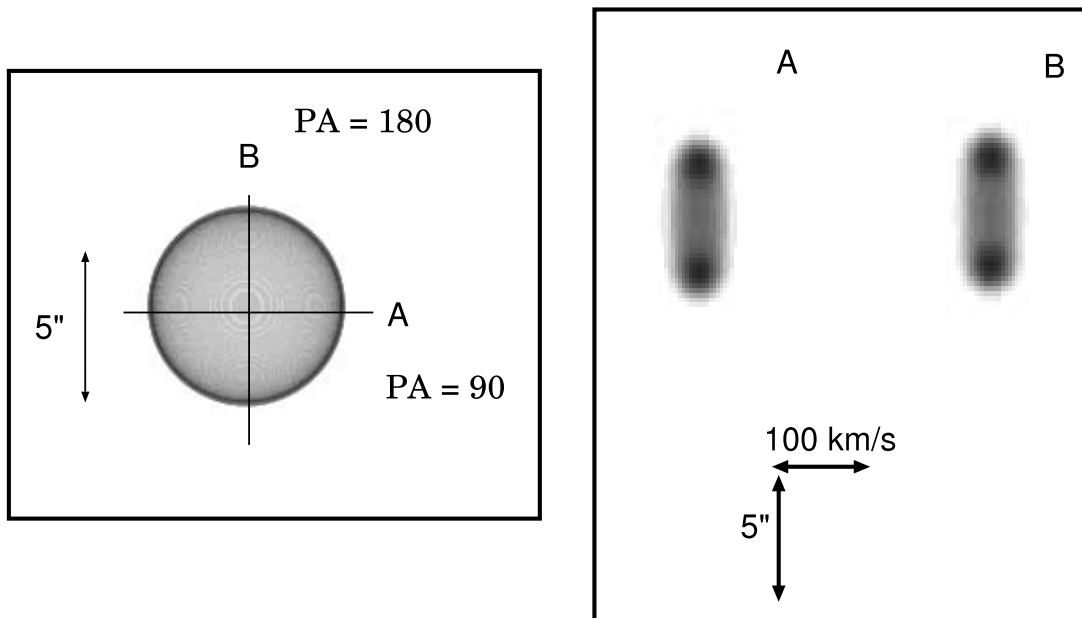


FIG. 8.—IC 3568 [N II] model image and spectra.

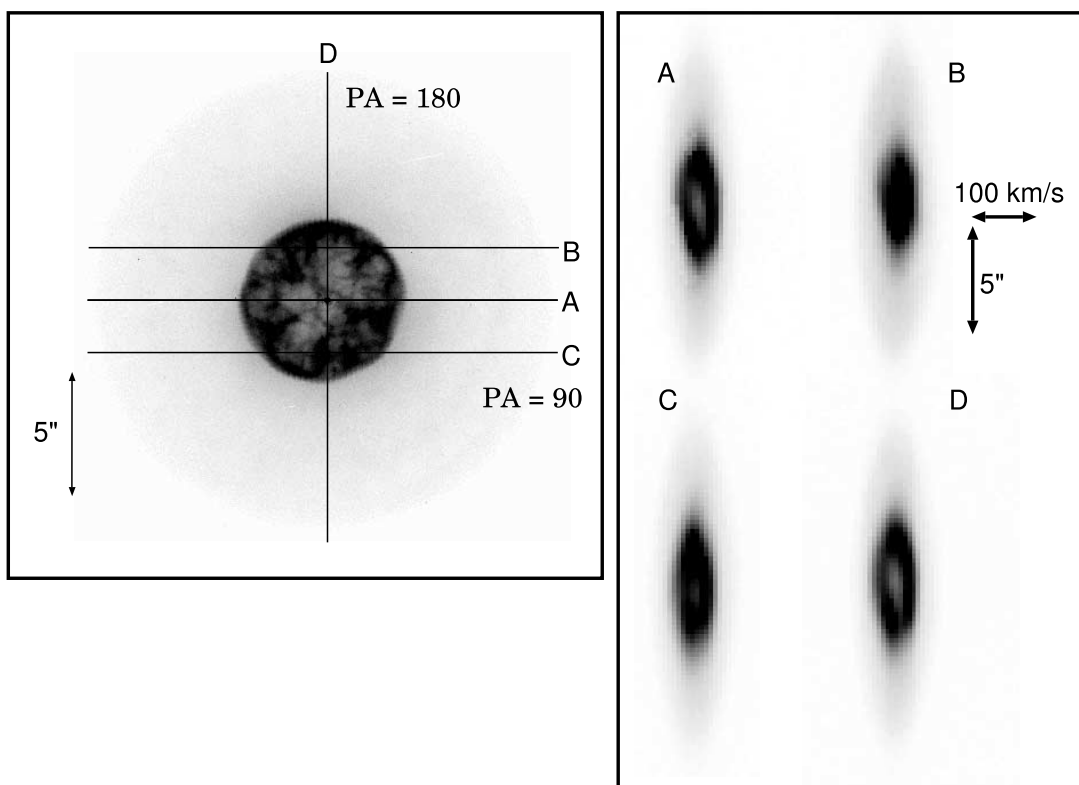


FIG. 9.—IC 3568 [O III] images from *HST* and spectra from KPNO 1999.

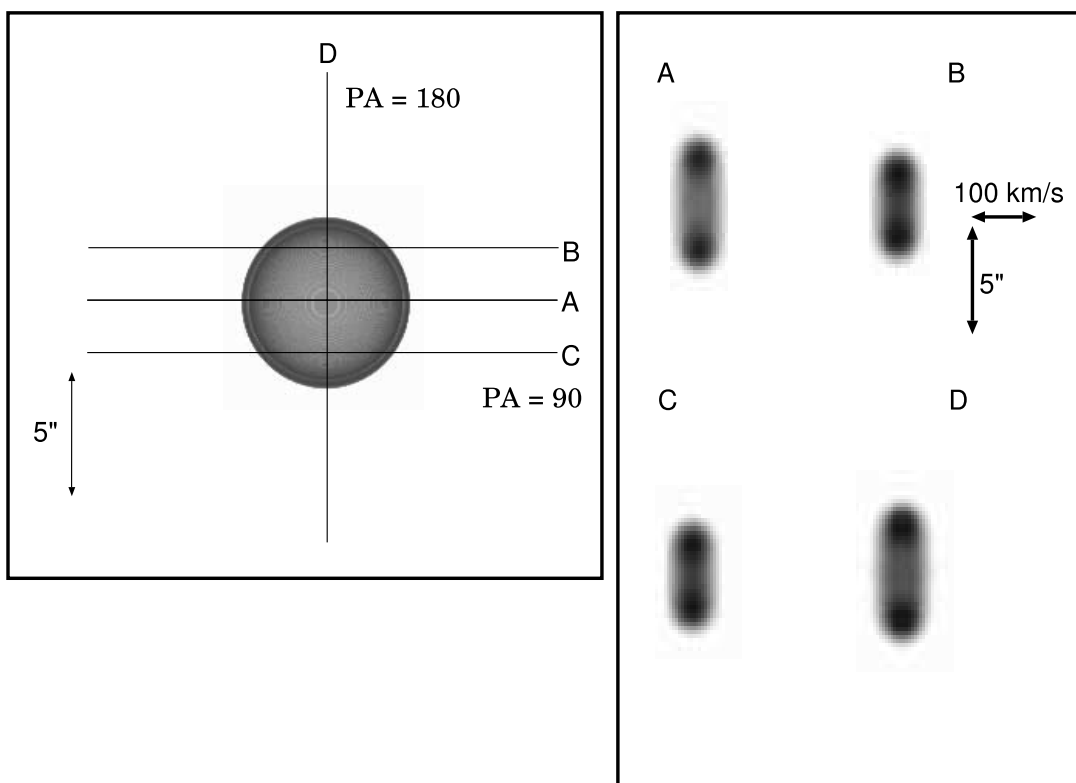


FIG. 10a

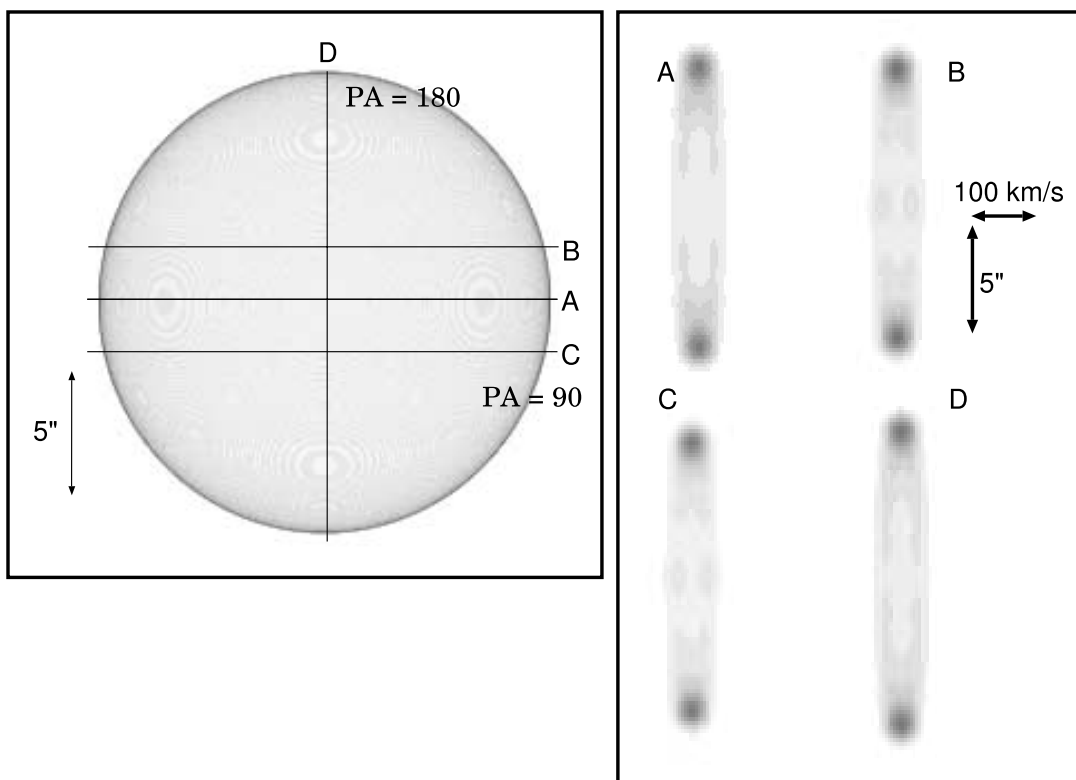


FIG. 10b

FIG. 10.—(a) IC 3568 [O III] core model image and spectra of the nebular core. (b) IC 3568 [O III] halo model image and spectra of the nebular halo.

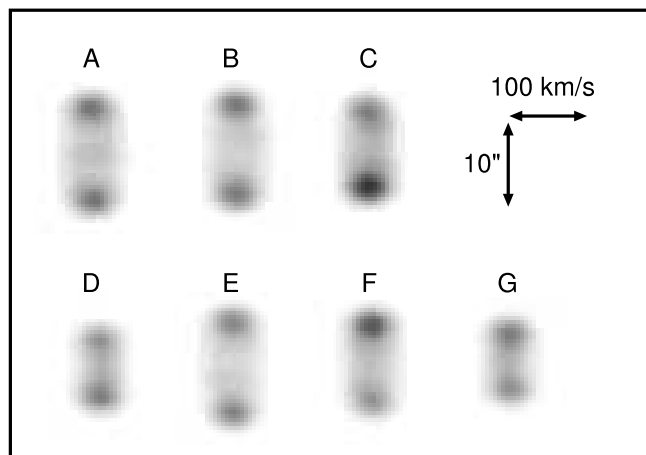
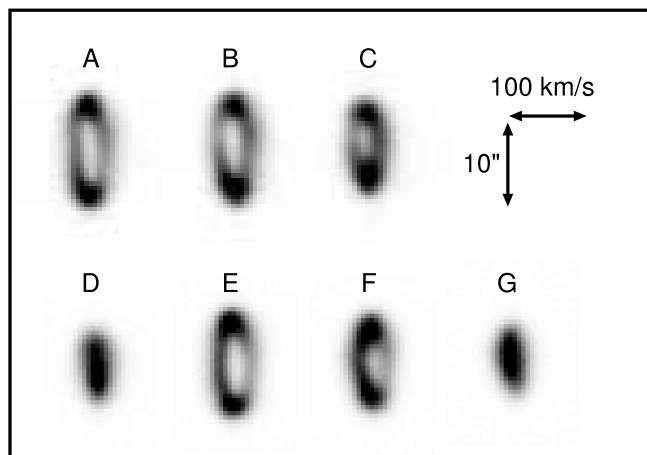
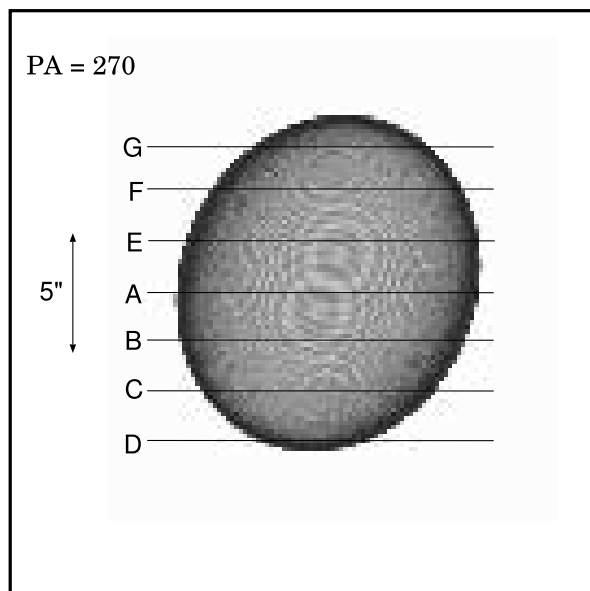
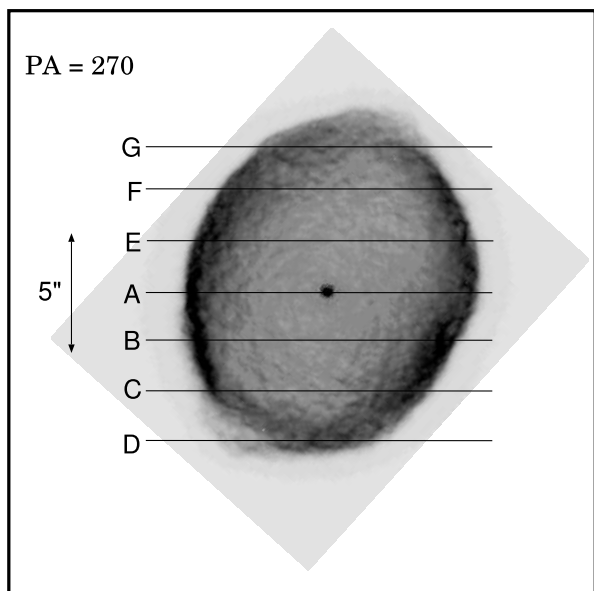


FIG. 11.—IC 418 [N II] images from *HST* and spectra from CTIO 1999.

FIG. 12.—IC 418 [N II] model image and spectra.

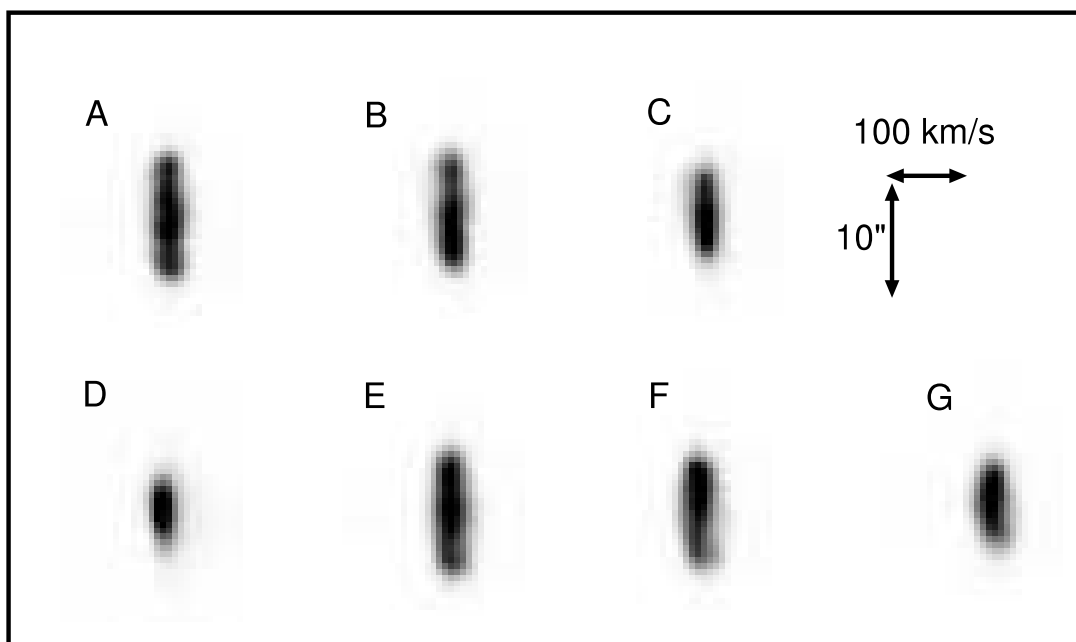
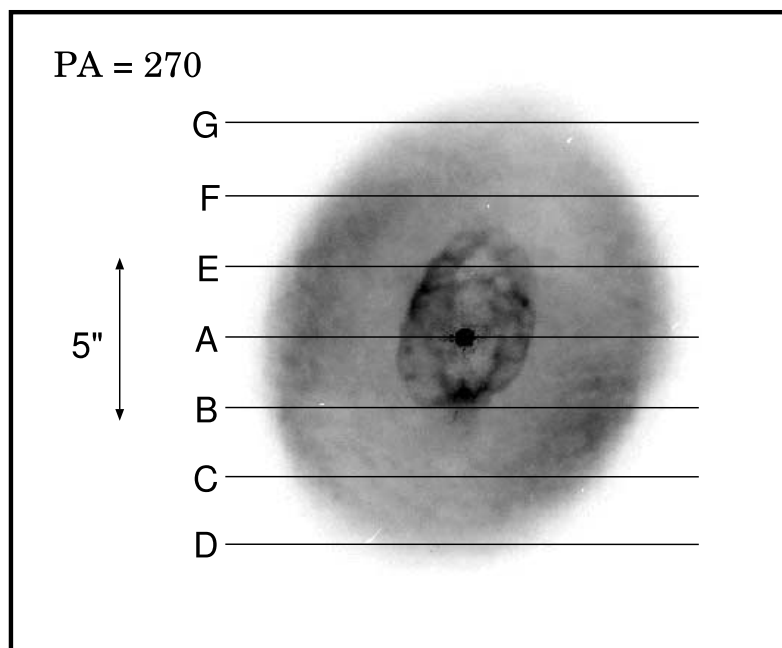


FIG. 13.—IC 418 [O III] images from *HST* and spectra from CTIO 1999.

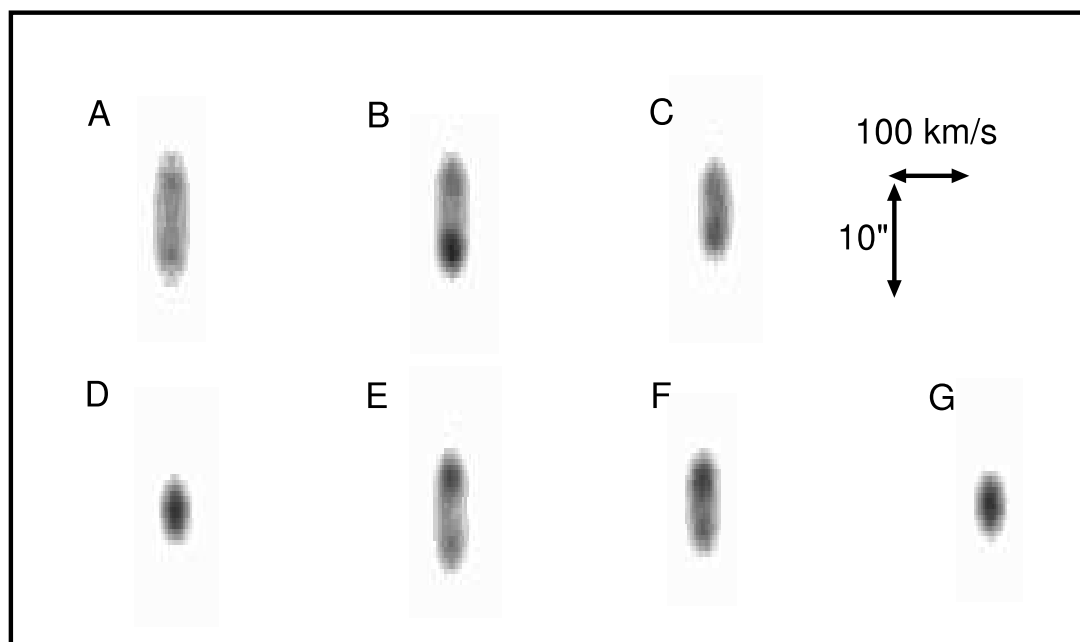
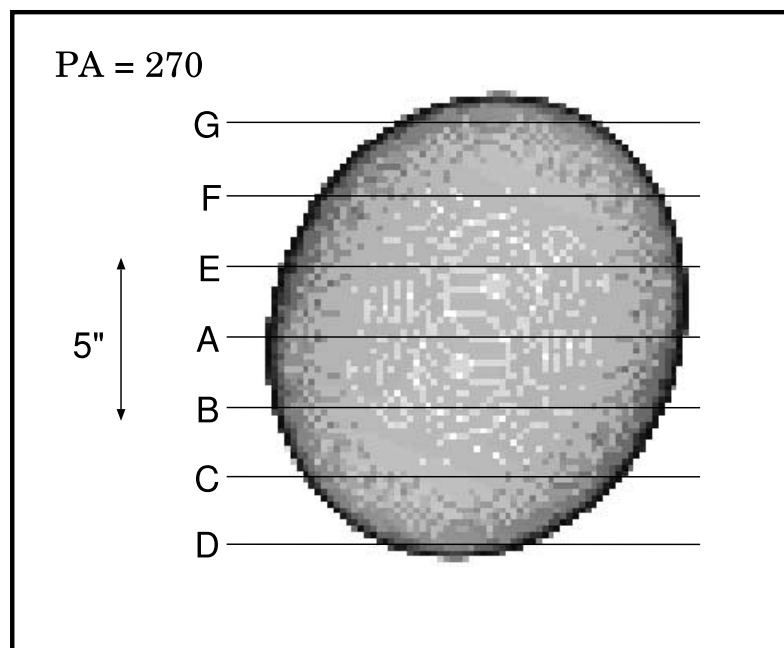


FIG. 14.—IC 418 [O III] model image and spectra.

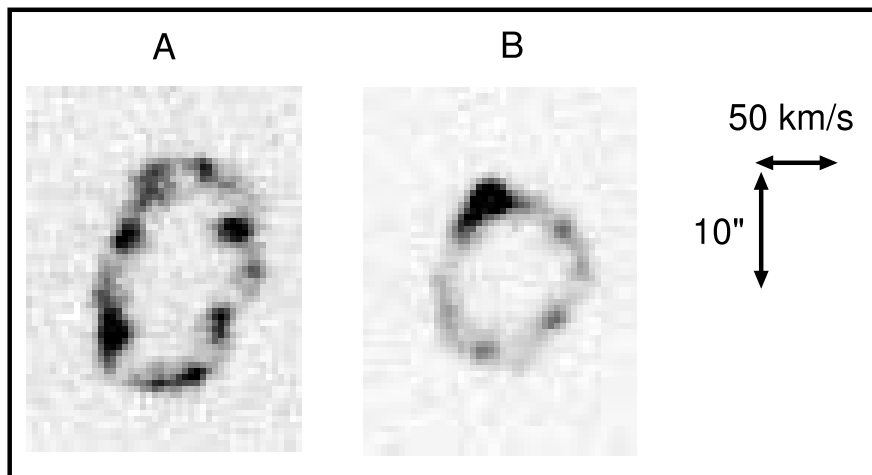
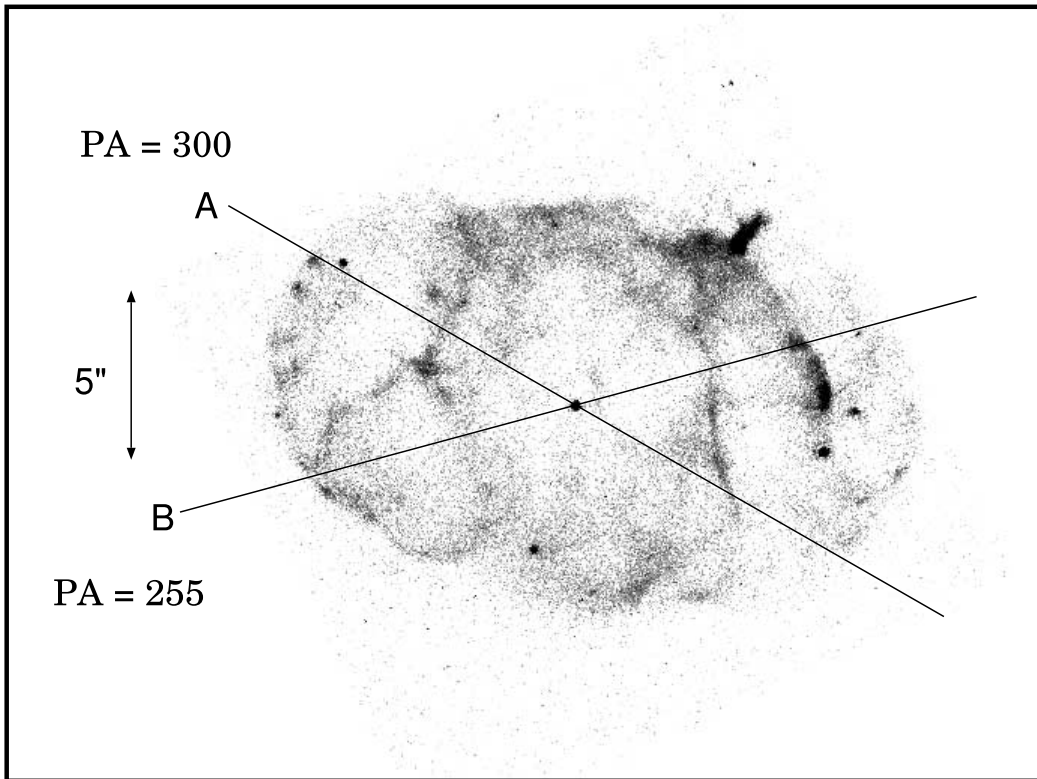


FIG. 15.—IC 4663 [N II] images from *HST* and spectra from CTIO 1999.

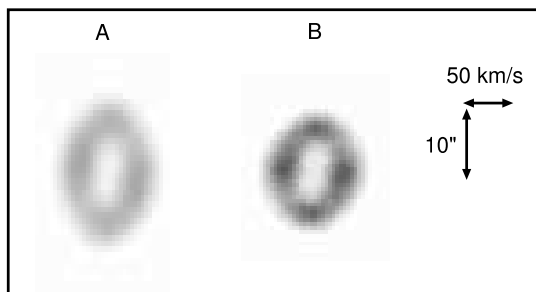
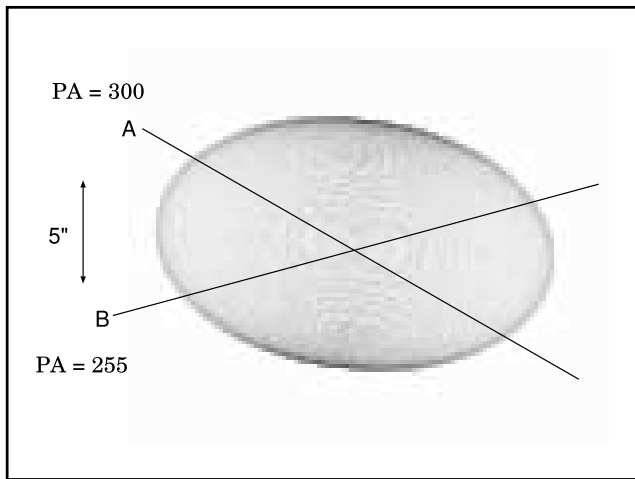


FIG. 16.—IC 4663 [N II] model image and spectra.

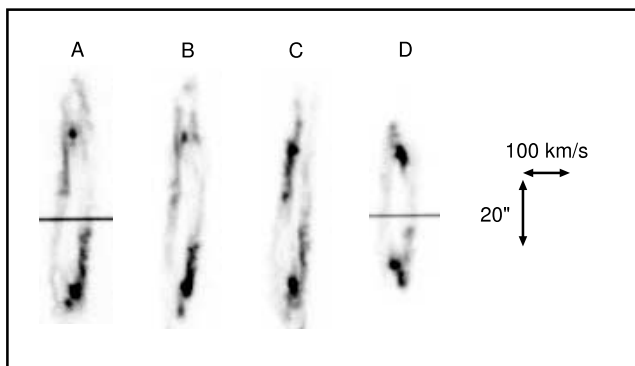
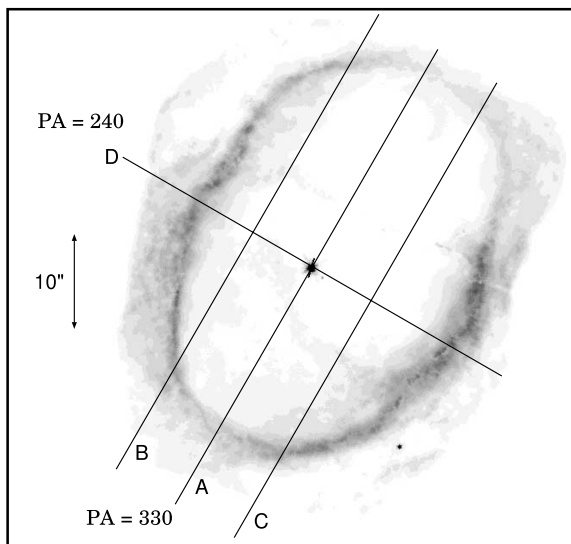


FIG. 17.—NGC 3132 [N II] images from *HST* and spectra from CTIO 1999.

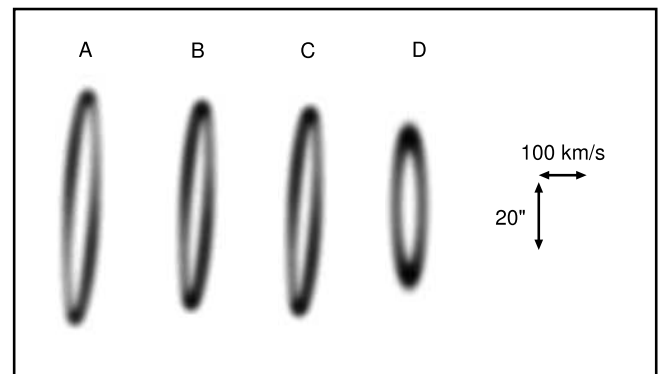
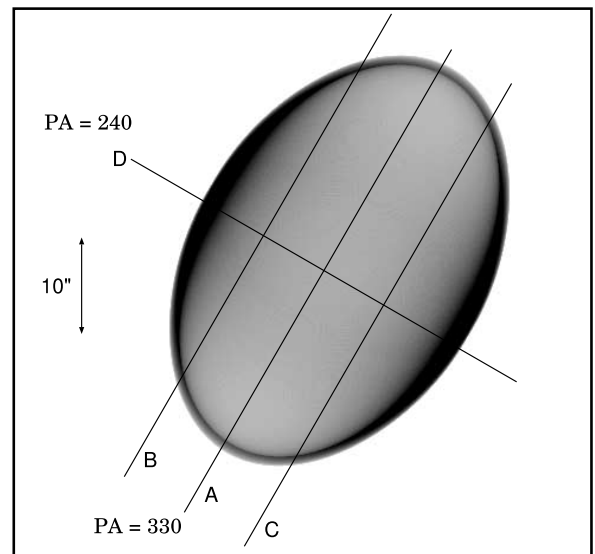


FIG. 18.—NGC 3132 [N II] model image and spectra.

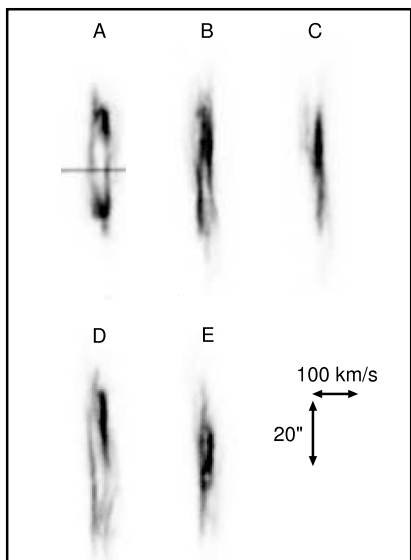
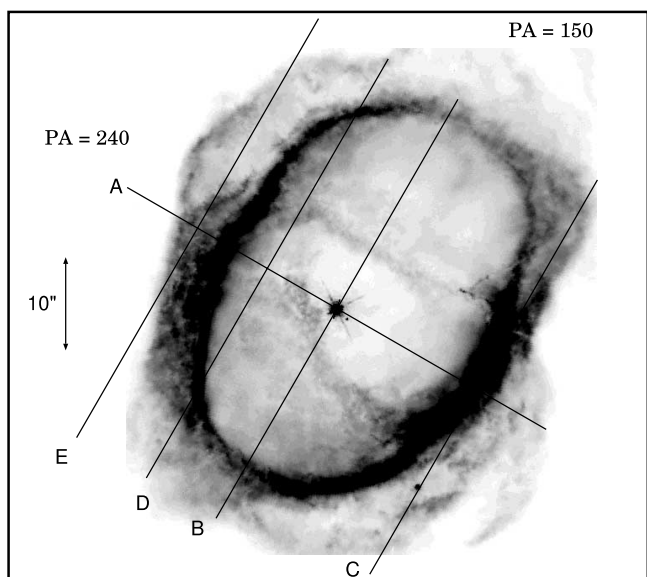


FIG. 19.—NGC 3132 [O III] images from *HST* and spectra from CTIO 1999.

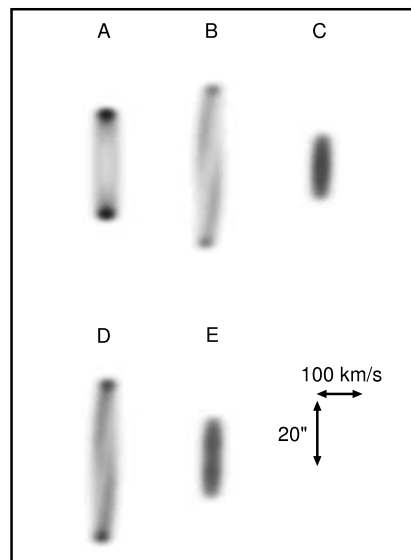
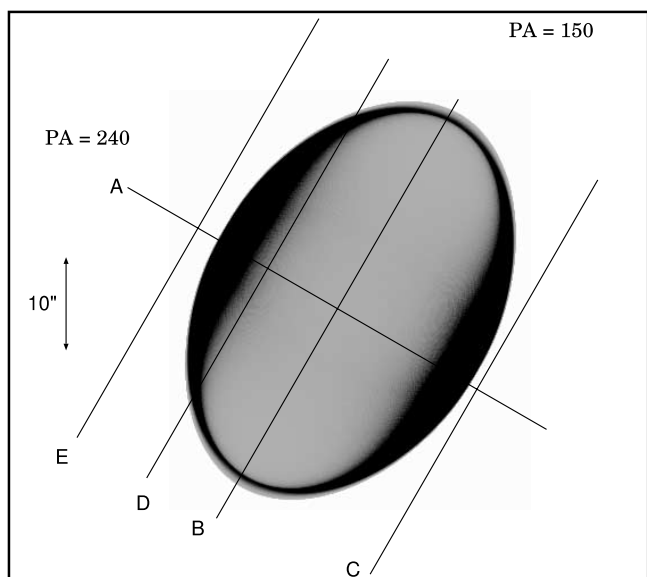


FIG. 20.—NGC 3132 [O III] model image and spectra.

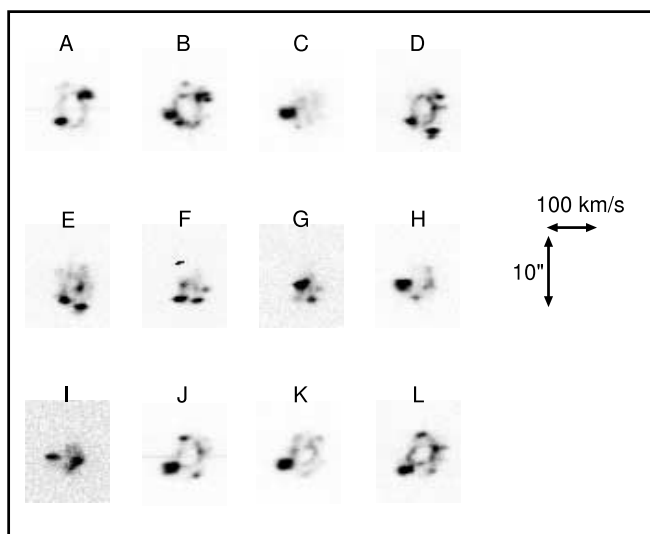
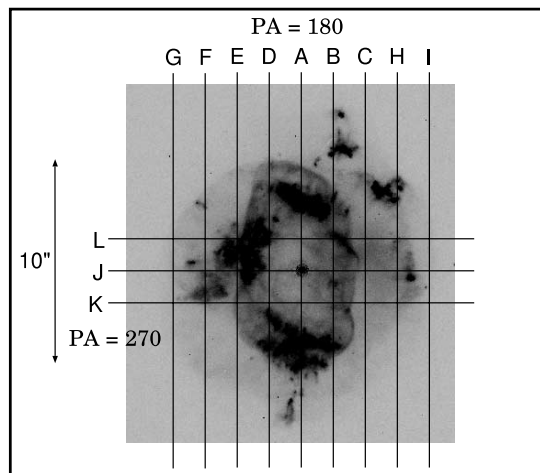


FIG. 21.—NGC 5882 [N II] images from *HST* and spectra from CTIO 1999.

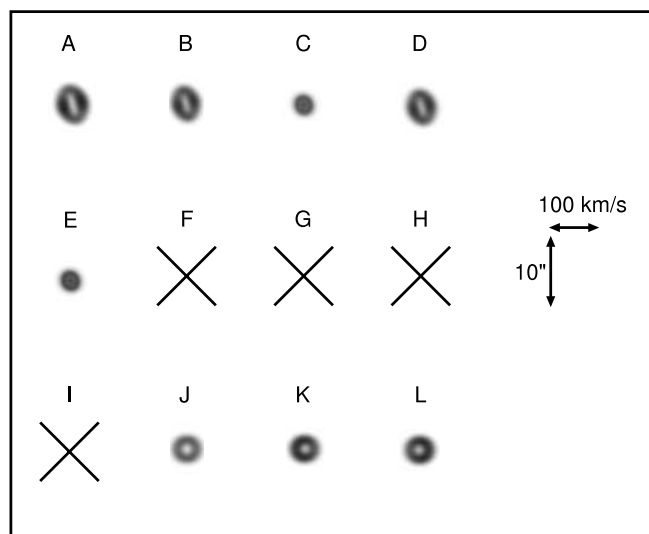
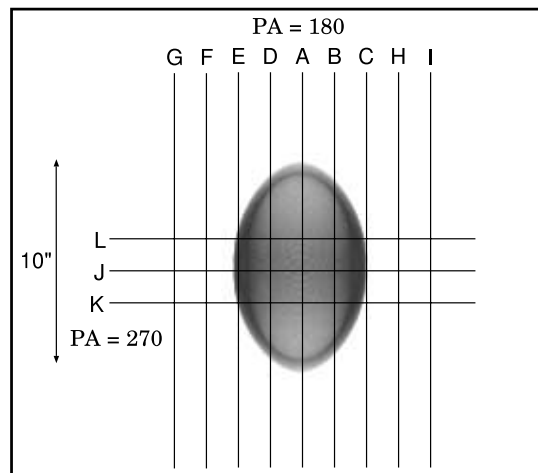


FIG. 22.—NGC 5882 [N II] model image and spectra.

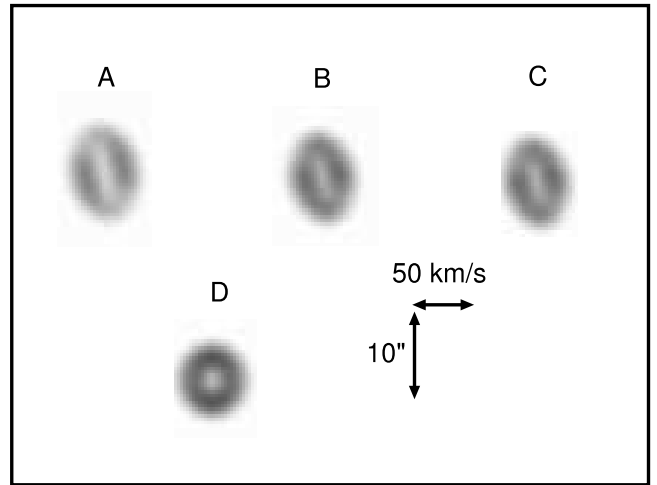
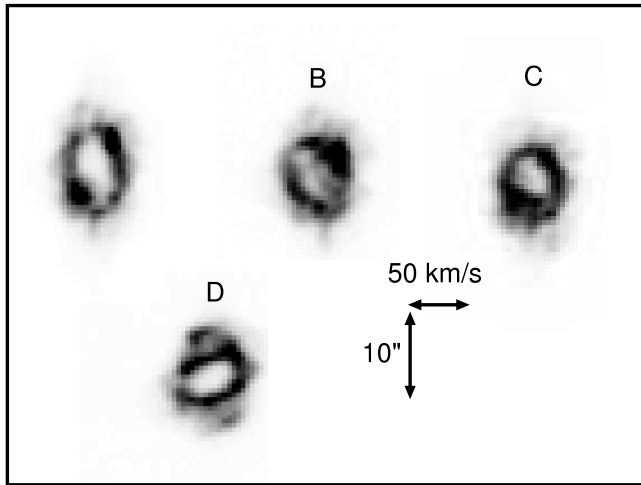
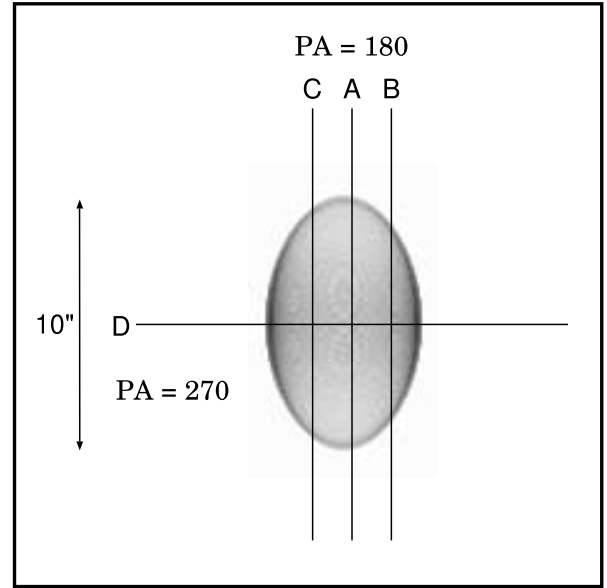
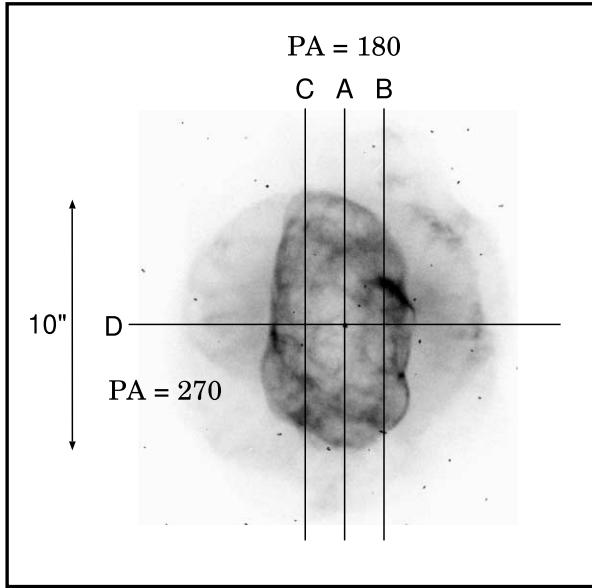


FIG. 23.—NGC 5882 [O III] images from *HST* and spectra from CTIO 1999.

FIG. 24.—NGC 5882 [O III] model image and spectra.

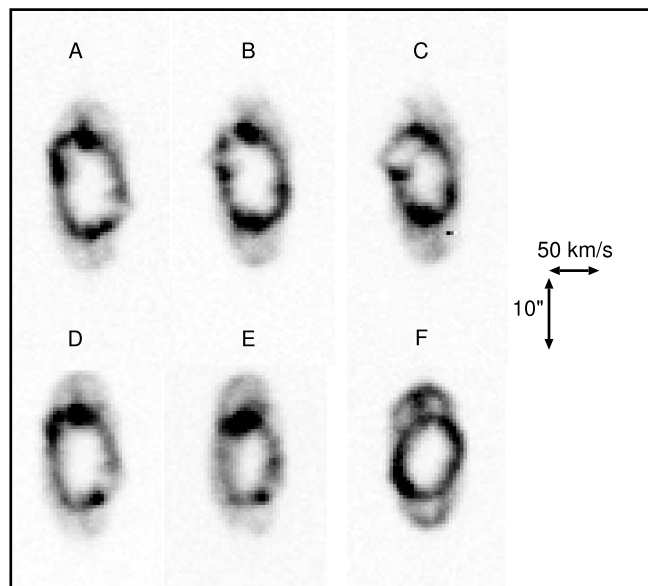
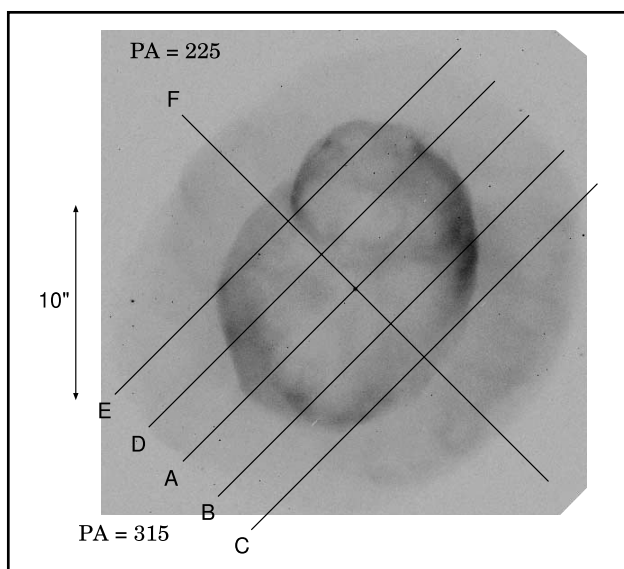


FIG. 25.—NGC 5979 [O III] images from *HST* and spectra from CTIO 1999.

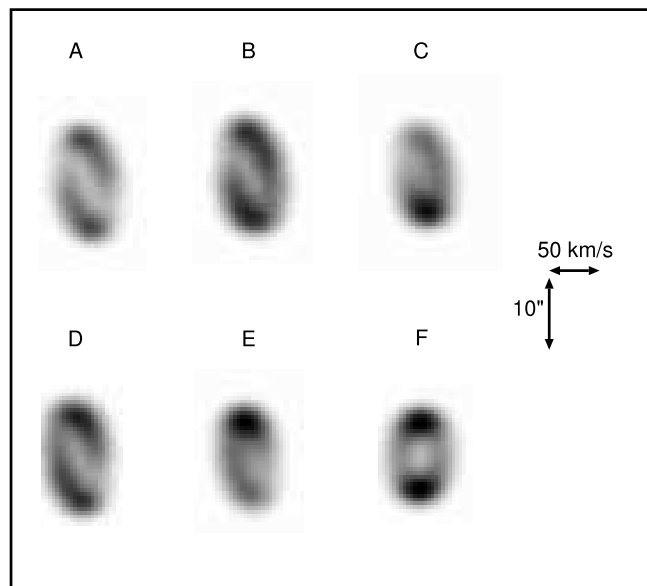
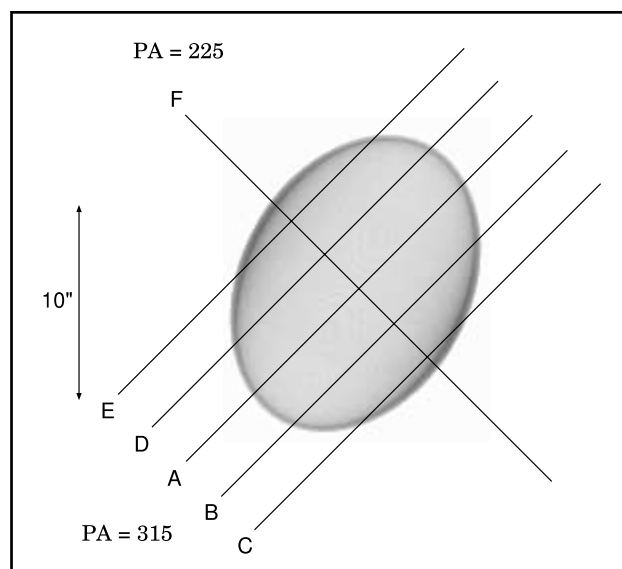


FIG. 26.—NGC 5979 [O III] model image and spectra.

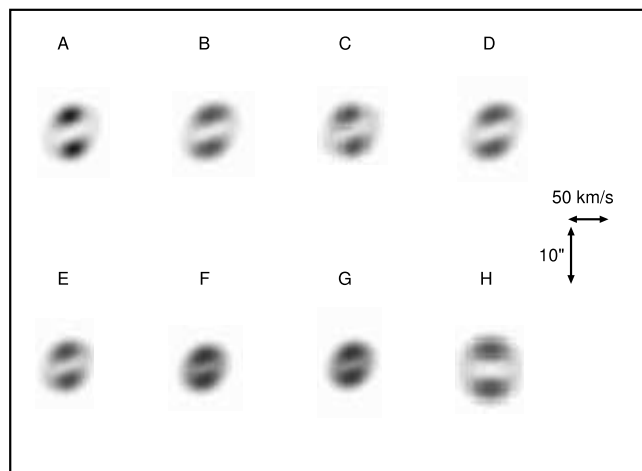
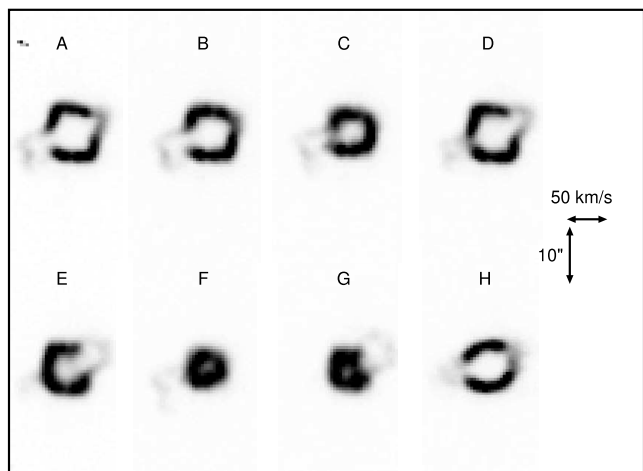
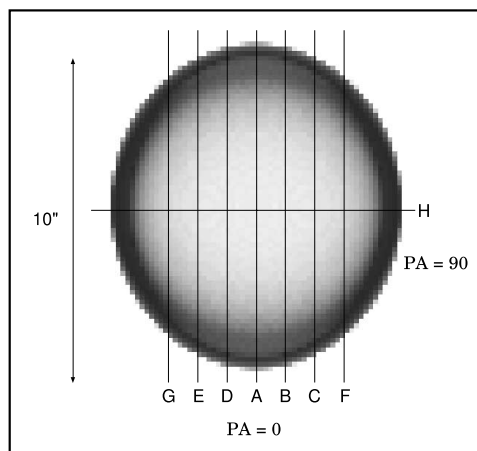
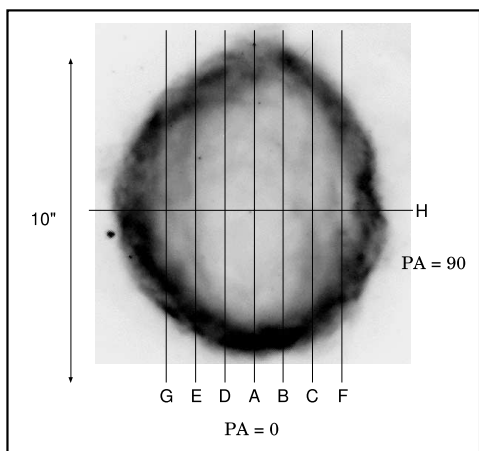


FIG. 27.—NGC 6565 [N II] images from *HST* and spectra from CTIO 1999.

FIG. 28.—NGC 6565 [N II] model image and spectra.

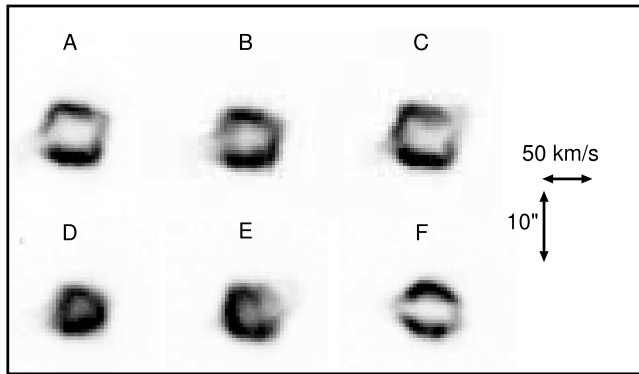
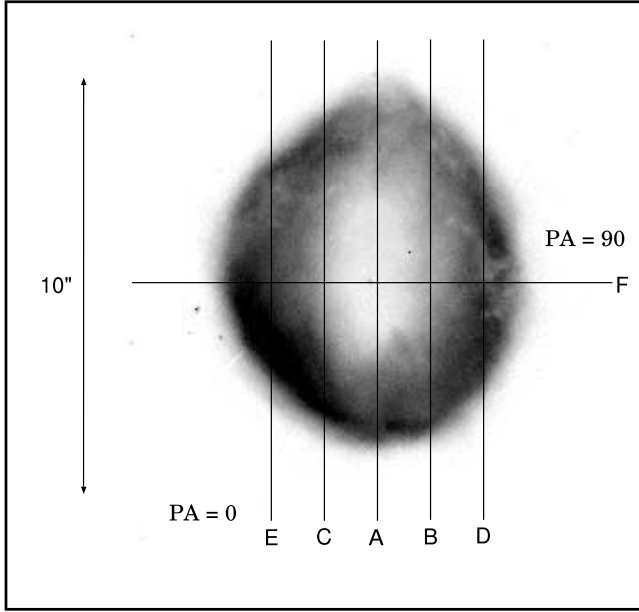


FIG. 29.—NGC 6565 [O III] images from *HST* and spectra from CTIO 1999.

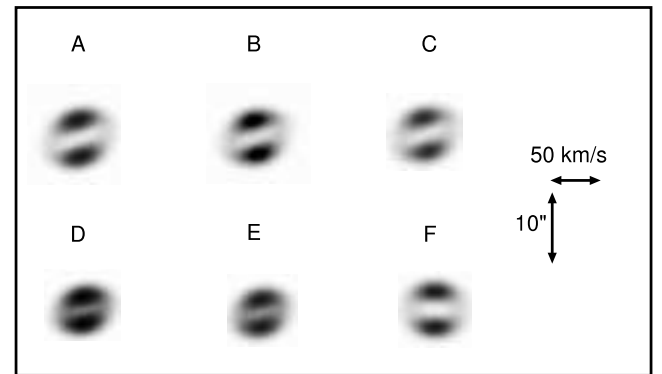
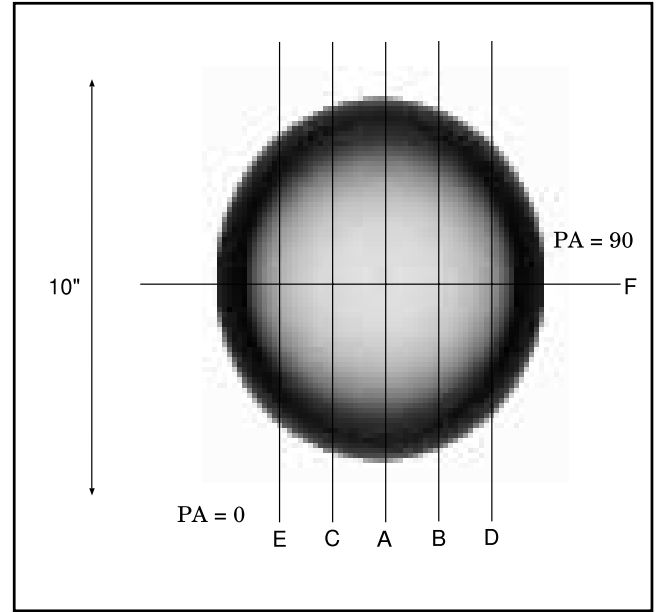


FIG. 30.—NGC 6565 [O III] model image and spectra.

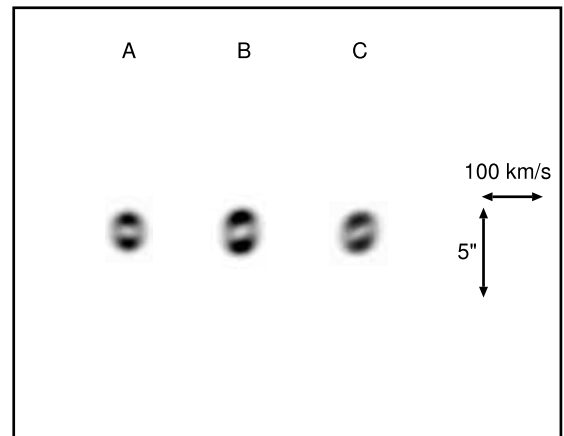
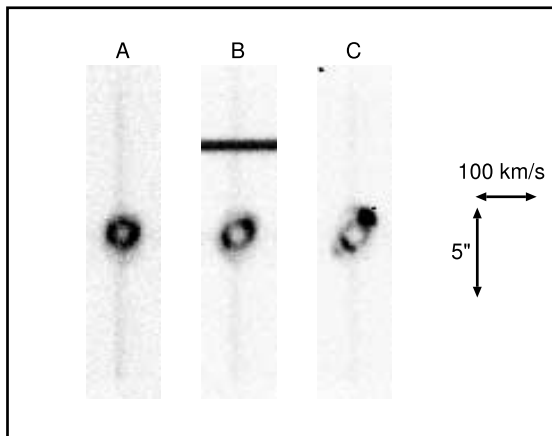
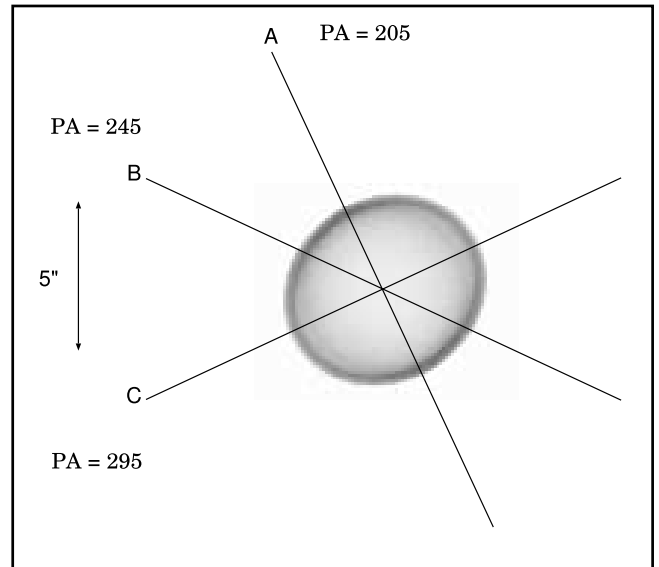
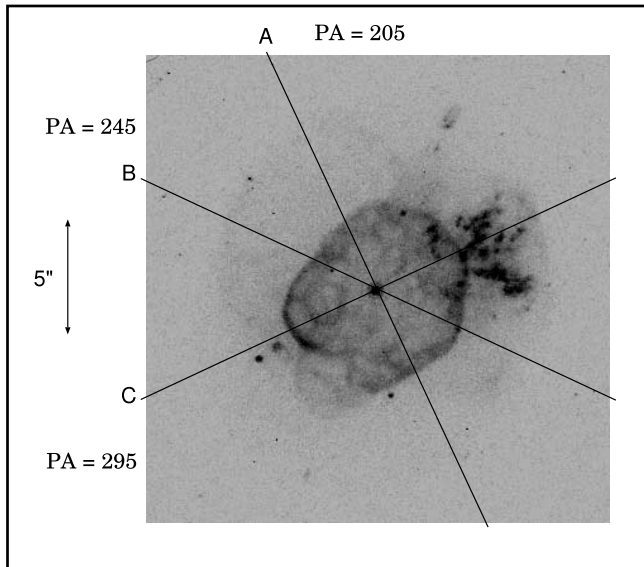


FIG. 31.—NGC 6578 [N II] images from *HST* and spectra from CTIO 2000.

FIG. 32.—NGC 6578 [N II] model image and spectra.

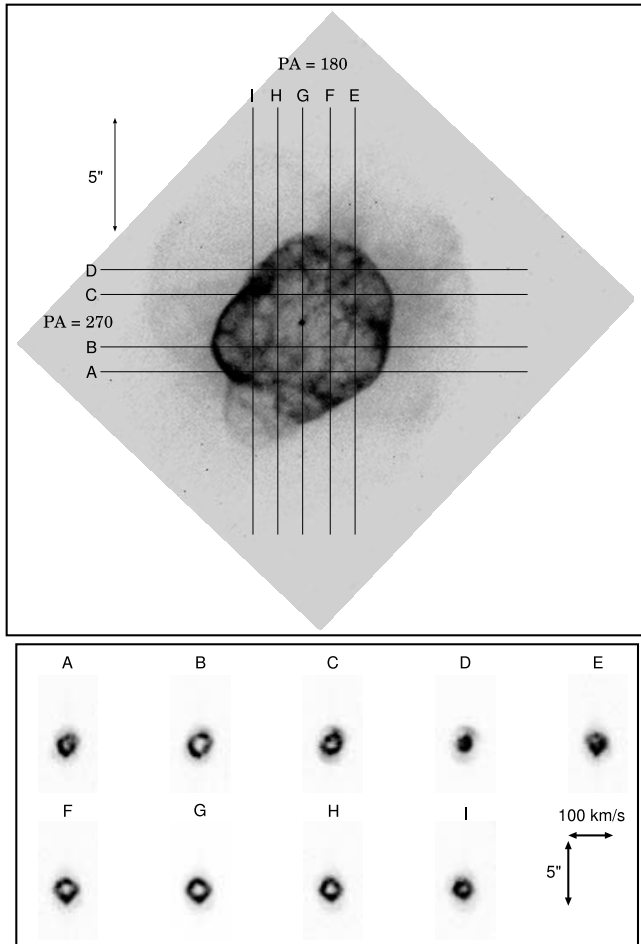


FIG. 33.—NGC 6578 [O III] images from *HST* and spectra from CTIO 1999.

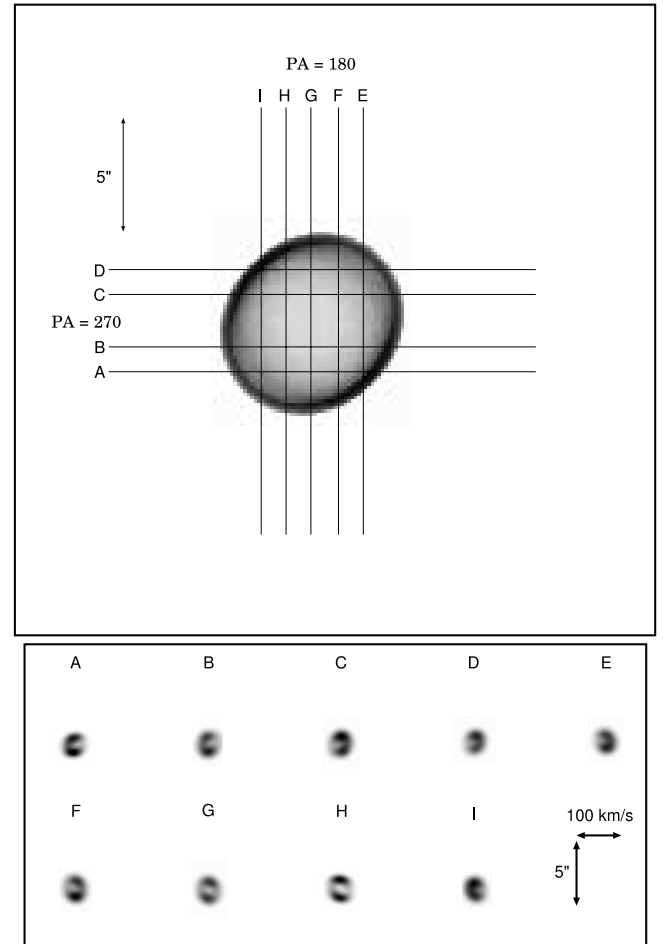


FIG. 34.—NGC 6578 [O III] model image and spectra.

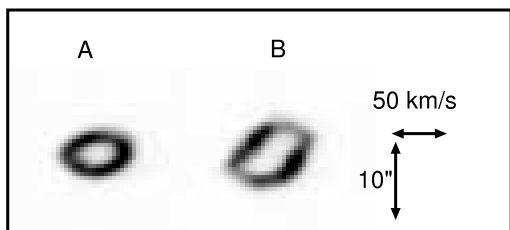
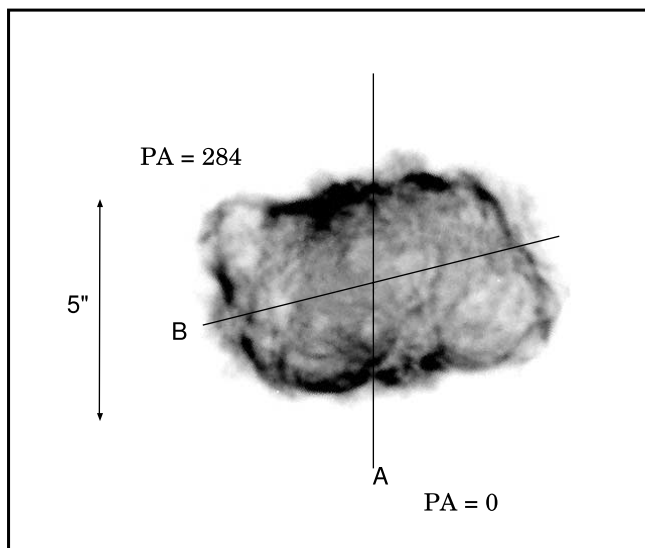


FIG. 35.—NGC 6741 [N II] images from *HST* and spectra from CTIO 1999.

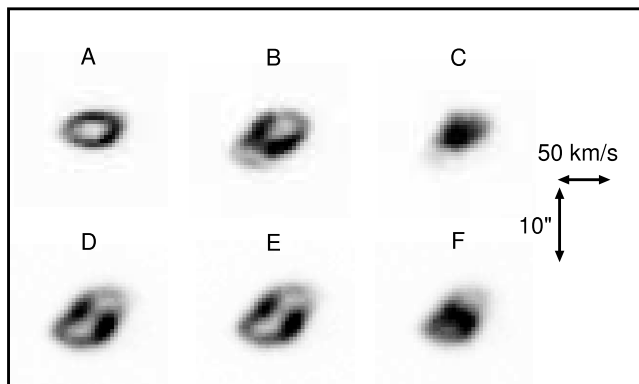
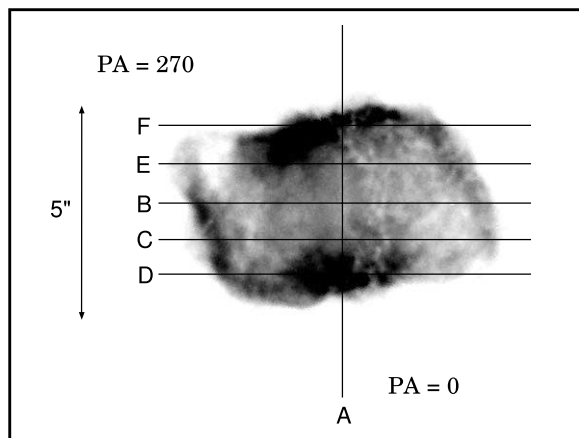


FIG. 37.—NGC 6741 [O III] images from *HST* and spectra from CTIO 1999.

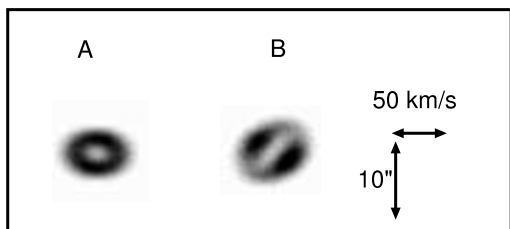
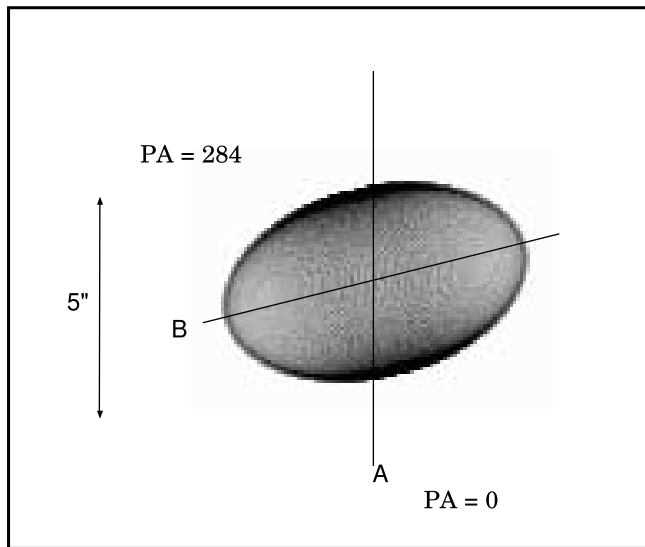


FIG. 36.—NGC 6741 [N II] model image and spectra.

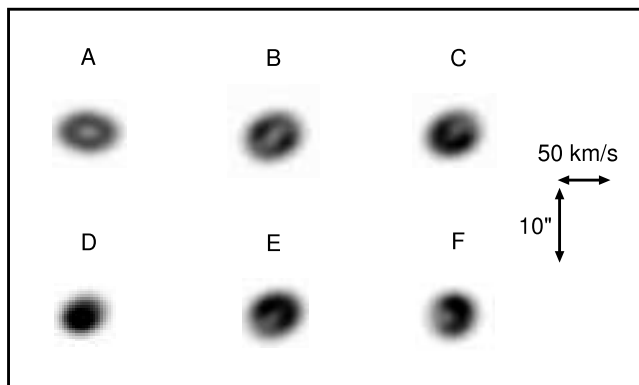
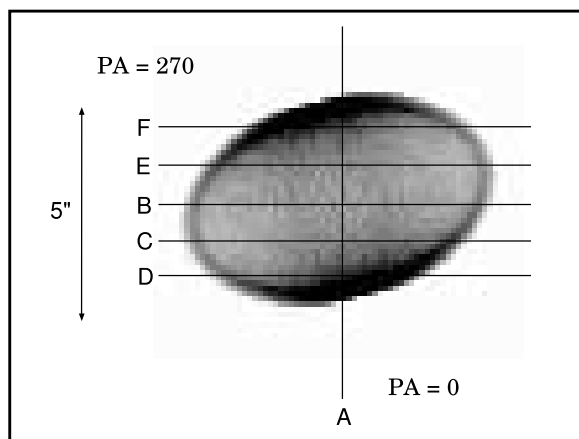


FIG. 38.—NGC 6741 [O III] model images and spectra.

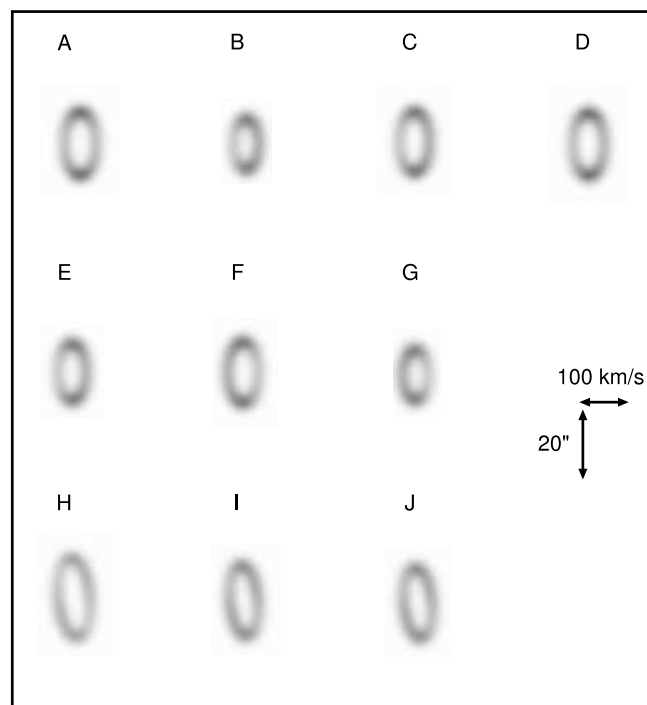
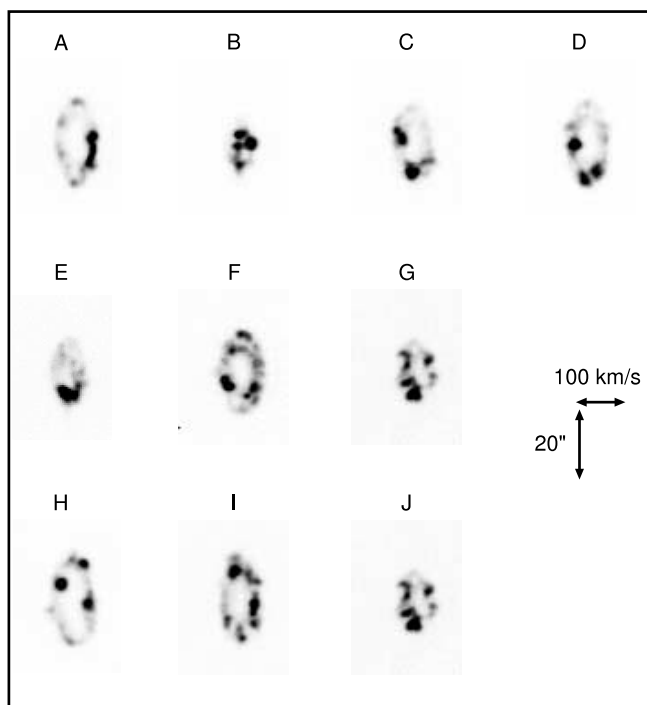
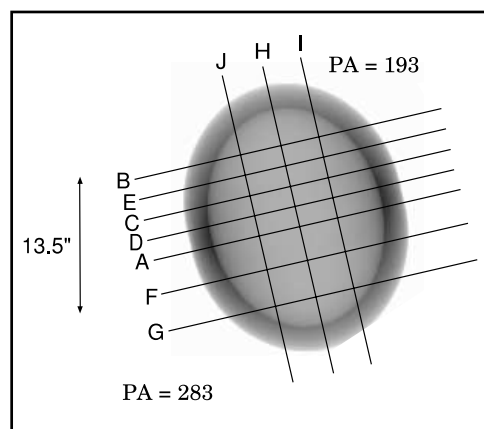
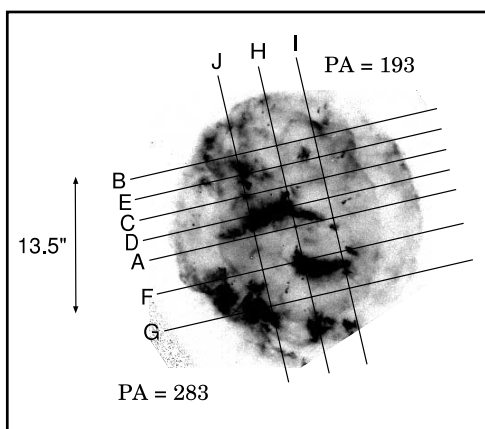


FIG. 39.—NGC 6818 [N II] images from *HST* and spectra from CTIO 1999.

FIG. 40.—NGC 6818 [N II] model image and spectra.

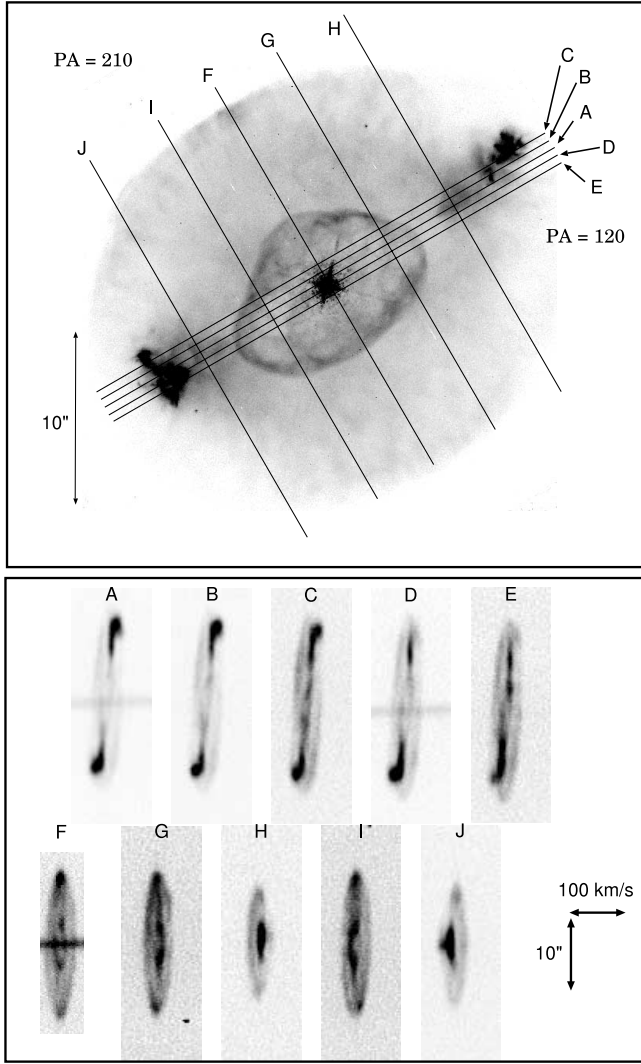


FIG. 41.—NGC 6826 [N II] images from *HST* and spectra from KPNO 1999.

For the kinematic portion of the model, we assumed that since all of the nebular gas was present at the location of the central star at some point in time, the expansion velocity of the gas is purely radial and the magnitude of the velocity is proportional to the distance from the central star.

3.2. Implementation of Fitting and Parameter Estimation

To implement the model described above, we begin with an ellipsoidal surface, R_i , in the frame of the PN defined by two parameters: the length of the major axis, $R_{i, \text{maj}}$, and the axial ratio, A_R . The third parameter is the ionization parameter, I_0 :

$$I_0 = \frac{dL/(d\Omega)}{(n_0 \eta \phi)^2 \alpha_B}, \quad (6)$$

which was used in conjunction with α , β , and γ to describe the density distribution and then to compute $R_0(\theta, \phi)$. We set the intensity at each voxel (volume element) equal to $\alpha_B n^2$ provided the voxel is between $R_i(\theta, \phi)$ and $R_0(\theta, \phi)$.

We then rotate the three-dimensional structure of the PN into the observer's frame using the angles i and θ' , which are the inclination relative to the line of sight and the position angle on the sky. The intensities are integrated along the line of sight to form

a two-dimensional model representing the brightness of the PN on the sky. Kinematic modeling requires the addition of a single parameter: the equatorial velocity, $v_0 = v(\pi/2, 0, R_i)$. The velocity in each voxel is oriented away from the central star, and the magnitude is proportional to the distance from the central star (normalized to v_0). After rotating the PN to the desired orientation, model long-slit spectra can be synthesized for each image pixel by integrating the intensity-weighted radial velocity for each voxel in the line of sight. In summary, an image model is uniquely defined by a selection of I_0 , α , β , γ , $R_{i, \text{maj}}$, A_R , i , and θ' , and the kinematic model requires v_0 in addition.

We generated synthetic images and spectra at the slit positions corresponding to the observed nebular major and minor axes. Since most of our PNe have thin shells, we adopted $\gamma = 0$ for all model realizations (see Zhang & Kwok 1998). To derive the “best-fit” model parameters, matches between model and data images/spectra were performed by eye. This method works well due to the orthogonality of the spatial and spectral data sets; the images constrain primarily the nebular structure orthogonal to the line of sight, while the spectra constrain nebular structures primarily along the line of sight. Although far from an optimal technique for matching models to data, Zhang & Kwok (1998) did the fits by eye as well. It is unclear whether a numerical technique for searching parameter space for the model that best matches the observed data is useful, since the PES model produces the most reasonable results in cases of approximately ellipsoidal shells (e.g., the relationship between radial velocity and radial structure is constrained by the ellipsoidal geometry).

For PNe with model fits, we display the best-fit model images and spectra following the data in Figures 1–56. Seven of the nine best-fit model parameters are listed in Table 3: we do not list R_i since the scale is arbitrary, and γ was not permitted to vary. Best-fit models were not made for some of the observed PNe due to the presence of complicated slit orientations, unresolved kinematic structure, and irregular nebular structure. Uncertainties in the fitted parameters were crudely estimated based on the quality of the model fits. To be specific, uncertainties were chosen by noting the positions in parameter space where the solution was an obvious mismatch to the data. In this way, we are probably overestimating the true errors in the parameters and have erred on the side of caution. We have assigned uncertainties to the axial ratios, inclination angles, and expansion velocities of 0.15, 10° , and 2 km s^{-1} , respectively. For those targets analyzed by Zhang & Kwok (1998) and in this work, we tabulate their best-fit parameters. The results from Zhang & Kwok (1998) were computed for the $\text{H}\alpha$ line, and as such are generally applicable to the $[\text{O III}]$ data sets in this paper. The exceptions are low-ionization, young PNe such as IC 418 or BD +30 –3639. The agreement between the $\text{H}\alpha$ and $[\text{N II}]$ data is expected to be somewhat worse, due mainly to the difference in ionization state between the two ions. Since $[\text{N II}]$ has a significantly lower ionization potential than $[\text{O III}]$, we expect the $[\text{N II}]$ emission to be farther away from the central stars, and this effect is visible in our results in most cases. In all of the cases examined in this paper, we find that the $[\text{N II}]$ gas has a larger apparent expansion velocity than the $[\text{O III}]$ gas. This inference is expected due to the lower ionization potential of the $[\text{N II}]$ and the generally larger distance of this gas from the central star.

The main differences between the Zhang & Kwok (1998) study and our analysis are due to (1) our use of higher spatial resolution image data (i.e., WFPC2 vs. ground-based) and (2) our inclusion of kinematic information in the PES model. The improved spatial resolution of our data results in more precise (and different) estimates of the shell thickness and in some cases, the

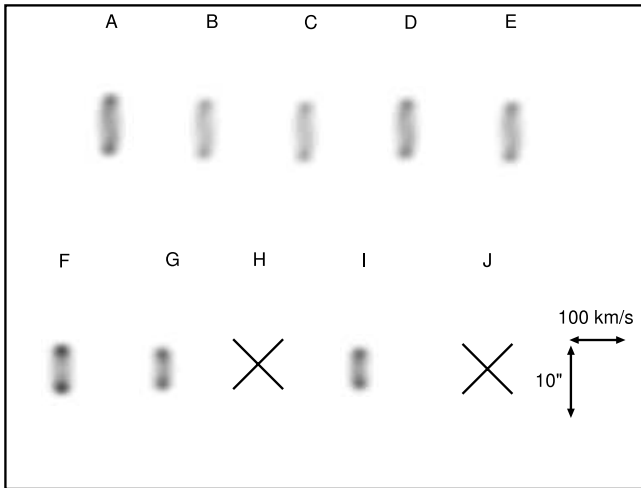
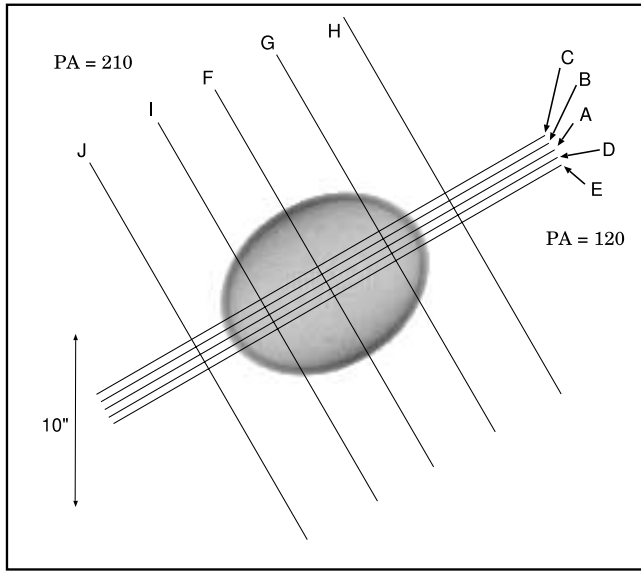


FIG. 42a

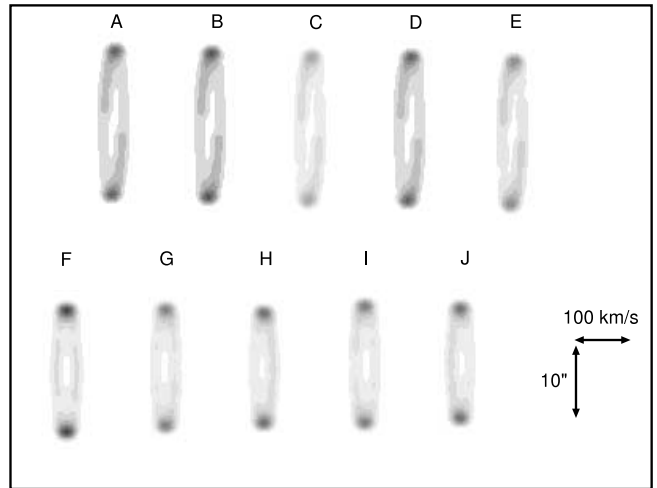
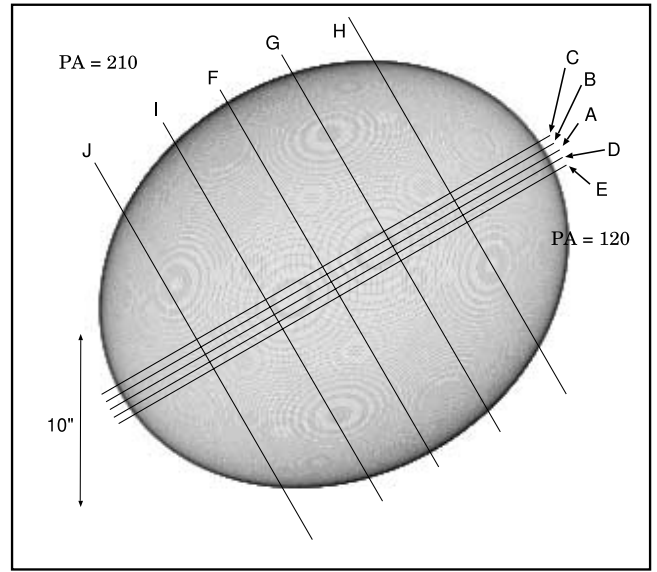


FIG. 42b

FIG. 42.—(a) NGC 6826 [N II] core model image and spectra of the nebular core. (b) NGC 6826 [N II] halo model image and spectra of the nebular halo.

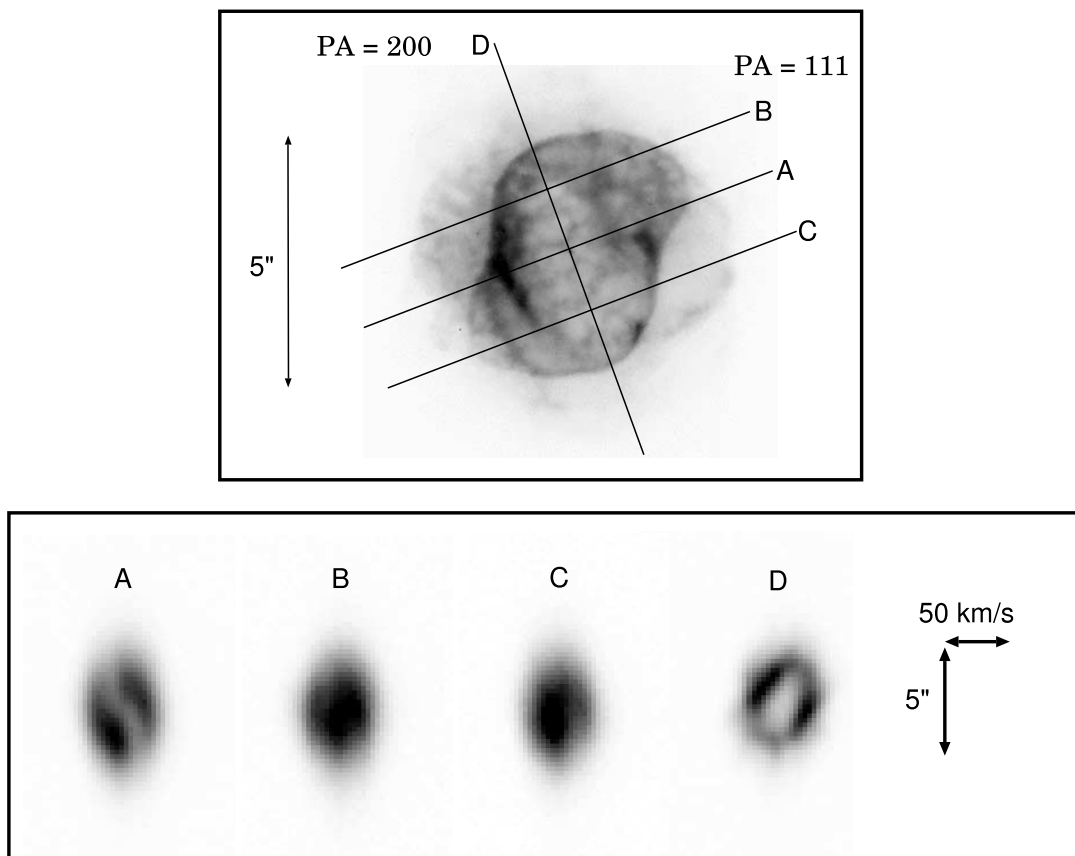


FIG. 43.—NGC 6884 [O III] images from *HST* and spectra from KPNO 1999.

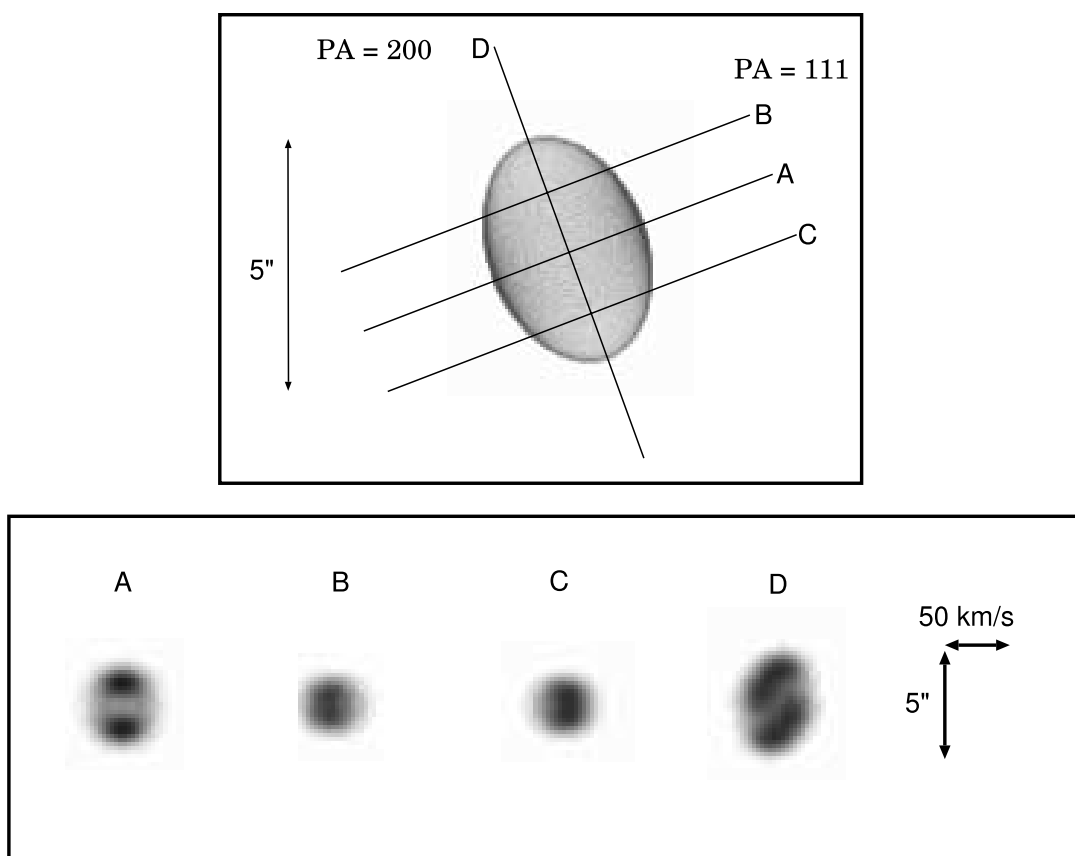


FIG. 44.—NGC 6884 [O III] model images and spectra.

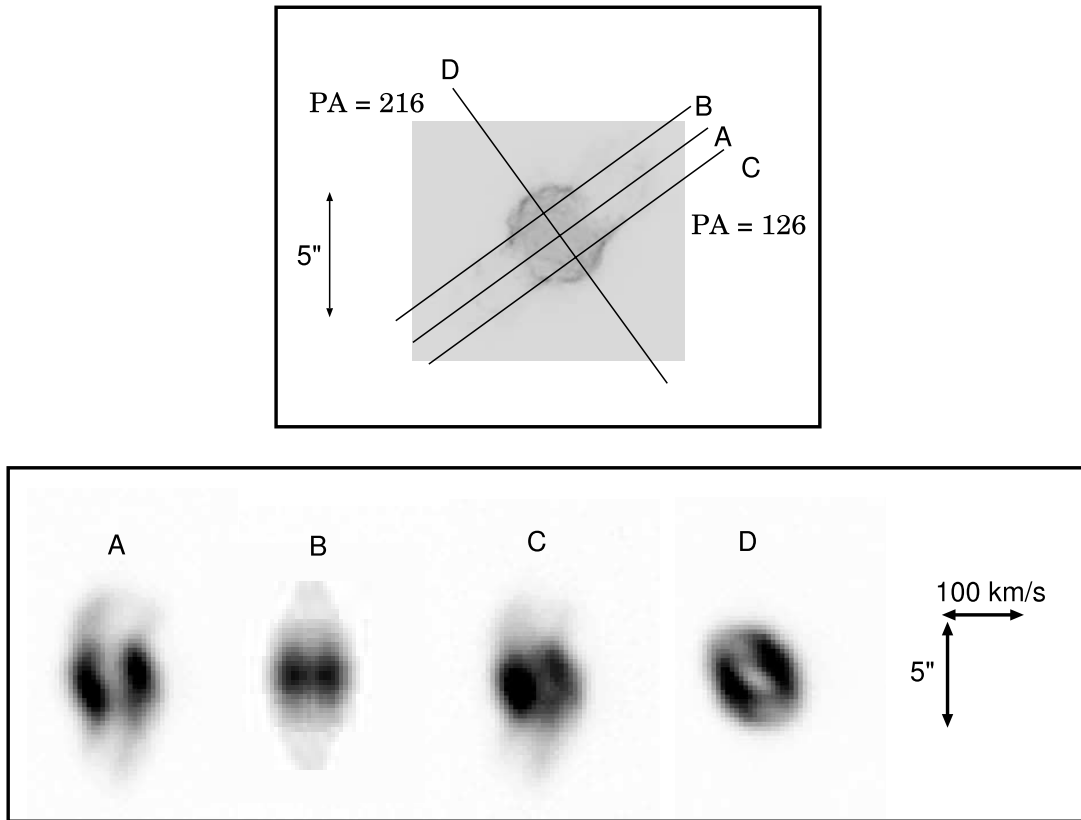


FIG. 45.—NGC 6886 [N II] images from *HST* and spectra from KPNO 1999.

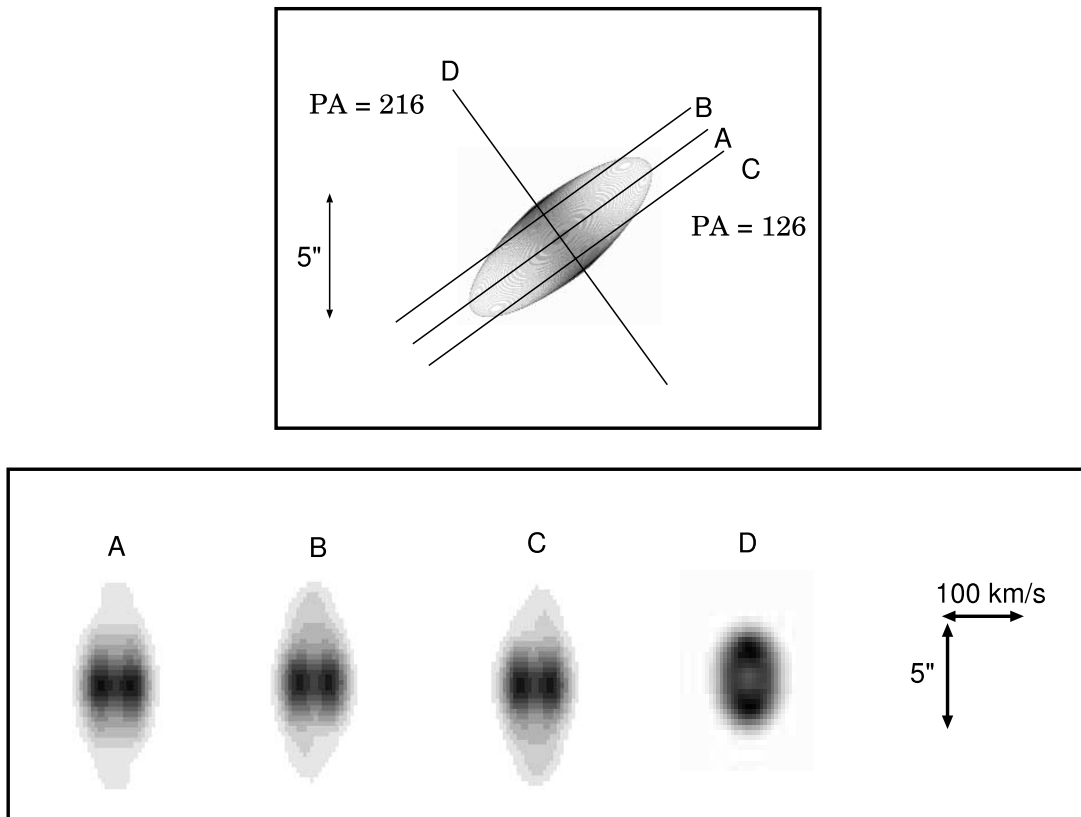


FIG. 46.—NGC 6886 [N II] model image and spectra.

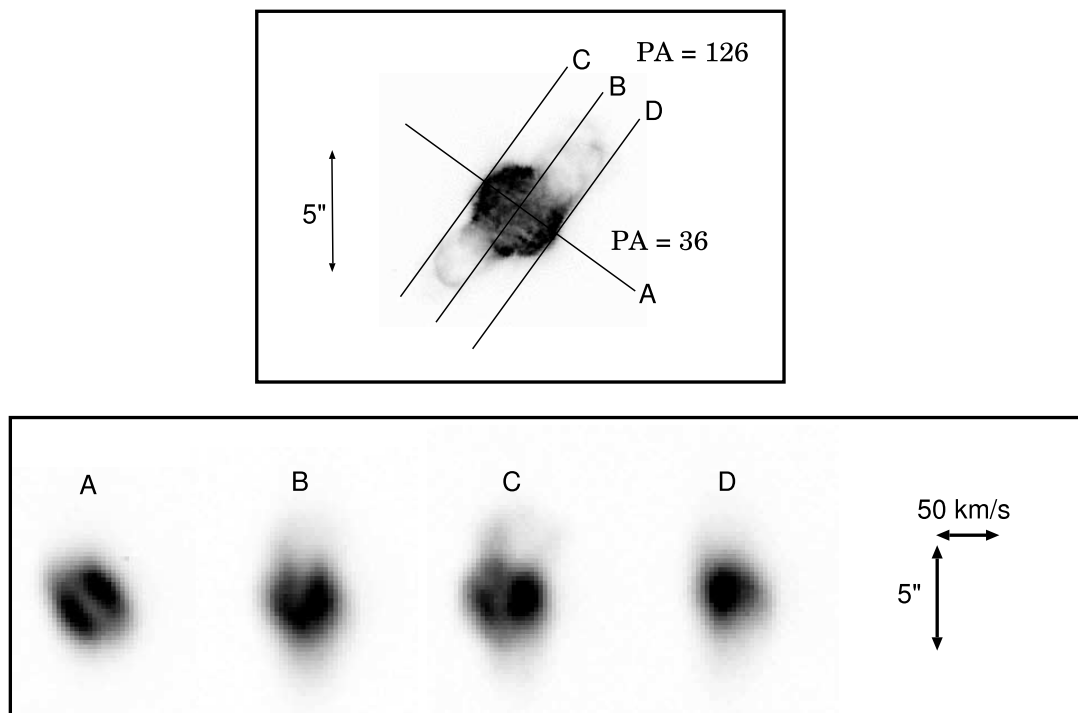


FIG. 47.—NGC 6886 [O III] images from *HST* and spectra from KPNO 1999.

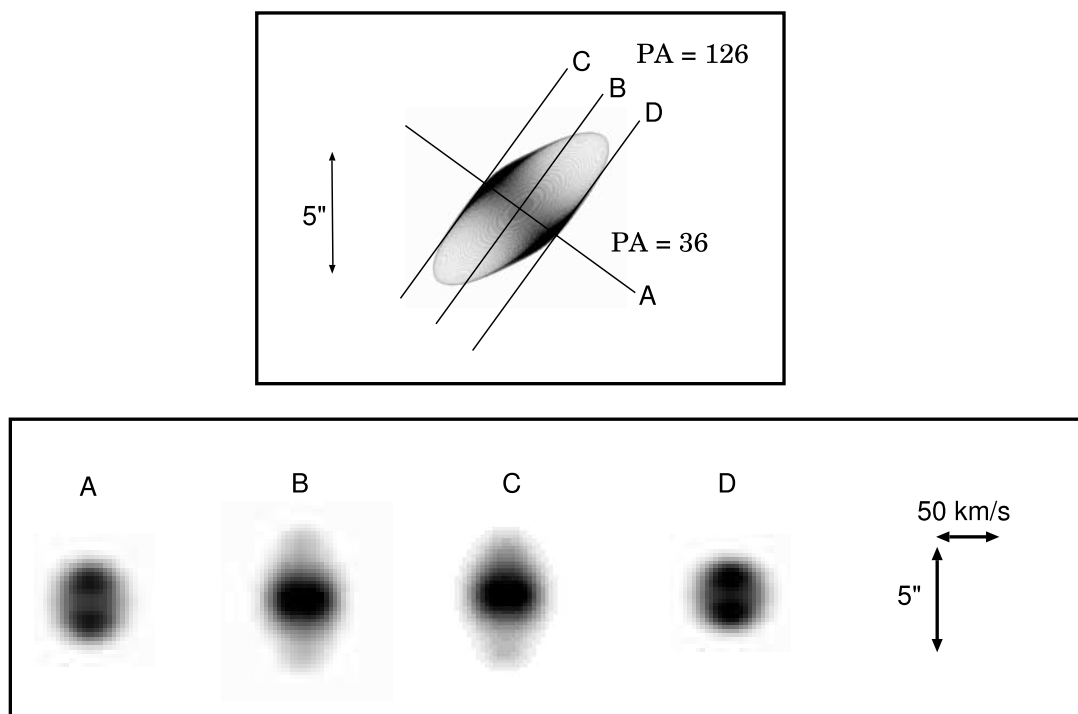


FIG. 48.—NGC 6886 [O III] model image and spectra.

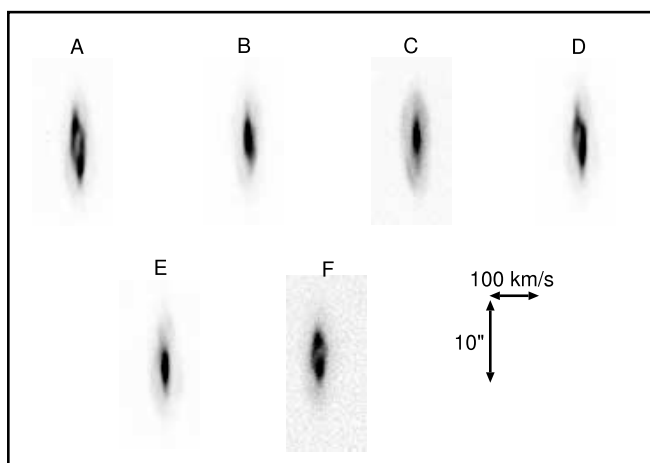
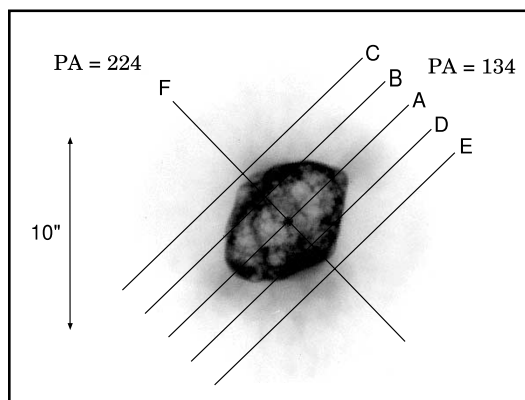


FIG. 49.—NGC 6891 [O III] images from *HST* and spectra from KPNO 1999.

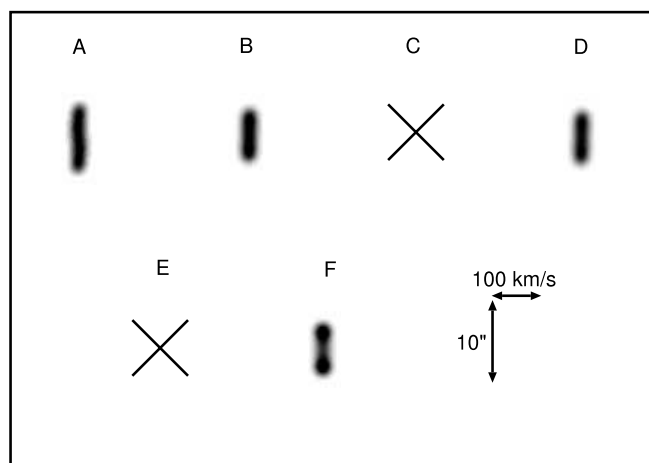
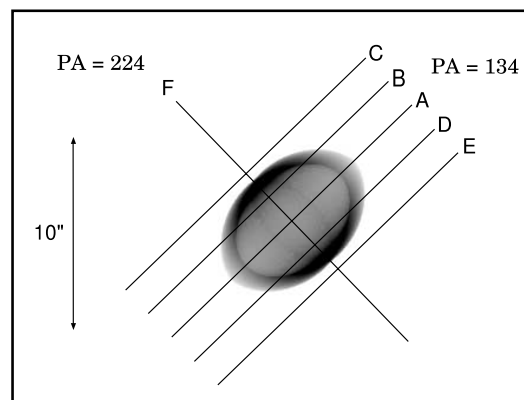


FIG. 50.—NGC 6891 [O III] model image and spectra.

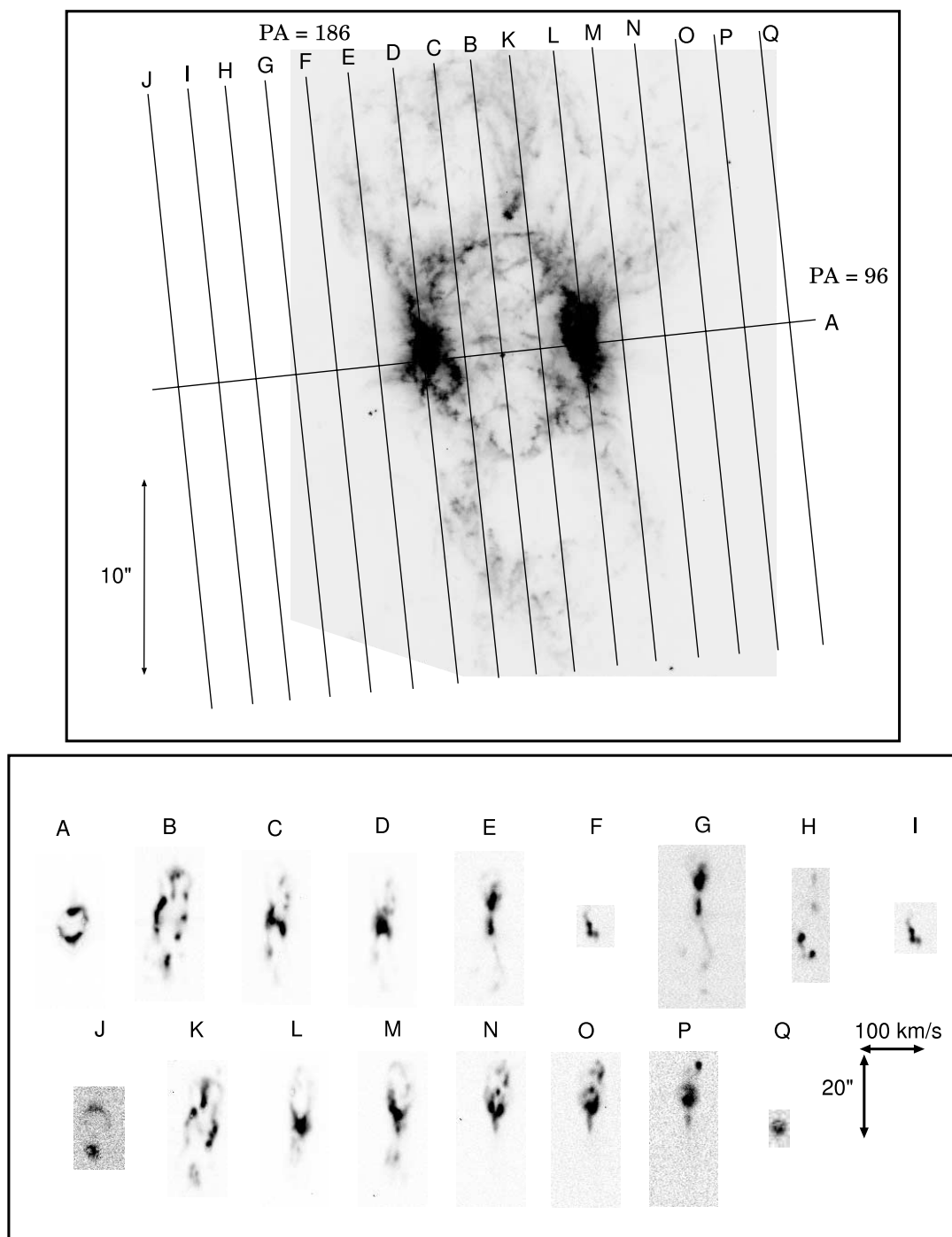


FIG. 51.—NGC 7026 [N II] images from *HST* and spectra from KPNO 1999.

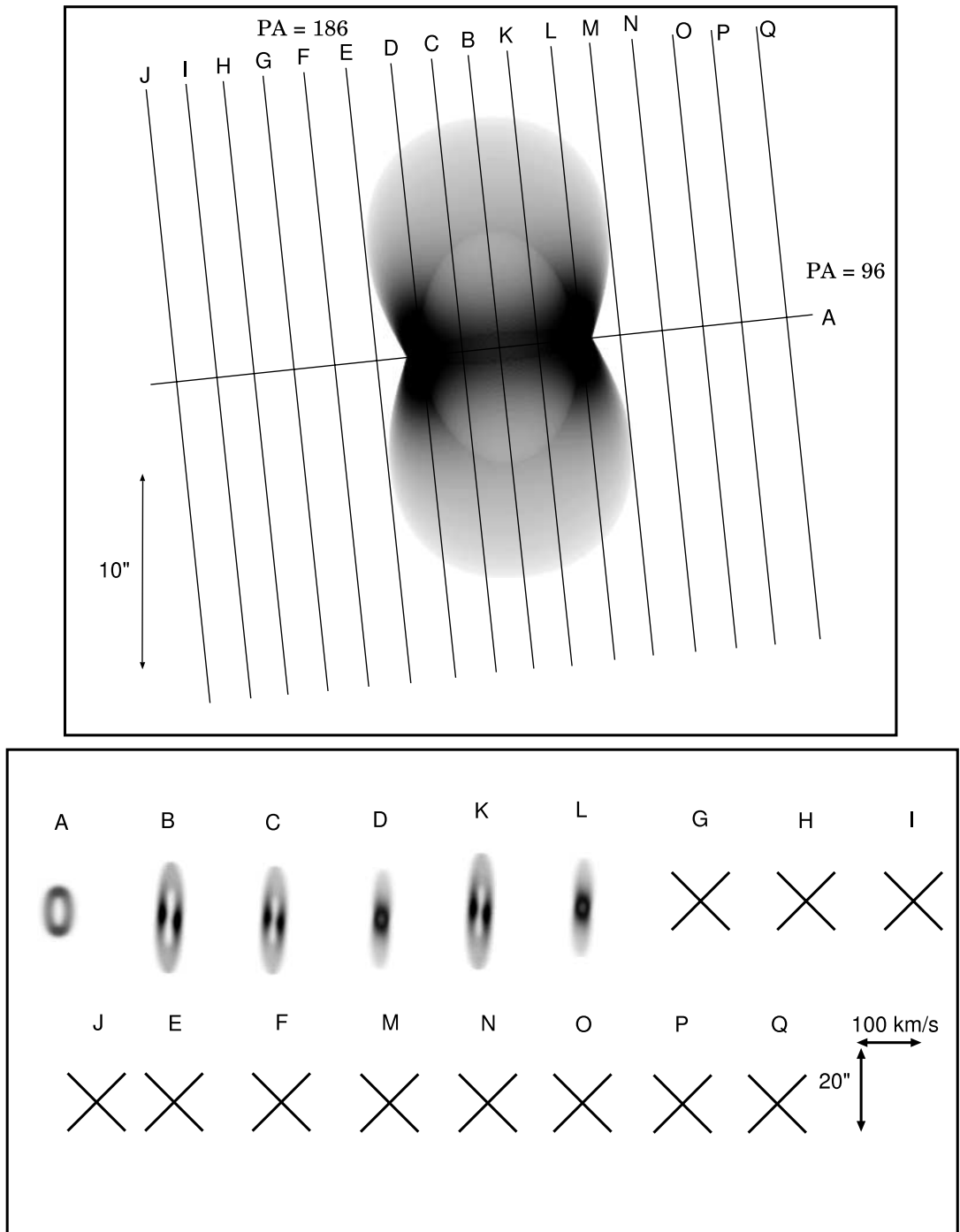


FIG. 52.—NGC 7026 [N II] model image and spectra.

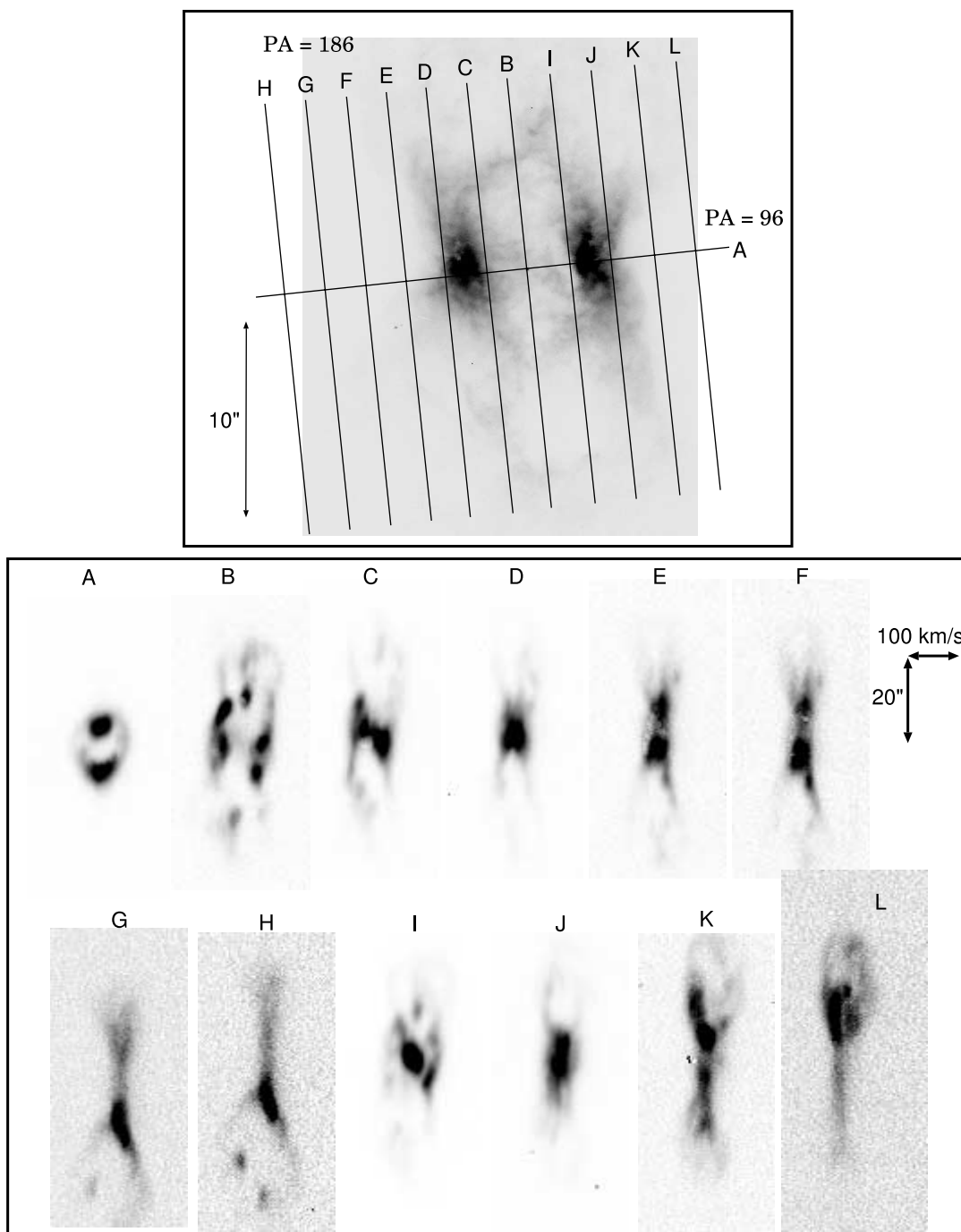


FIG. 53.—NGC 7026 [O III] images from *HST* and spectra from KPNO 1999.

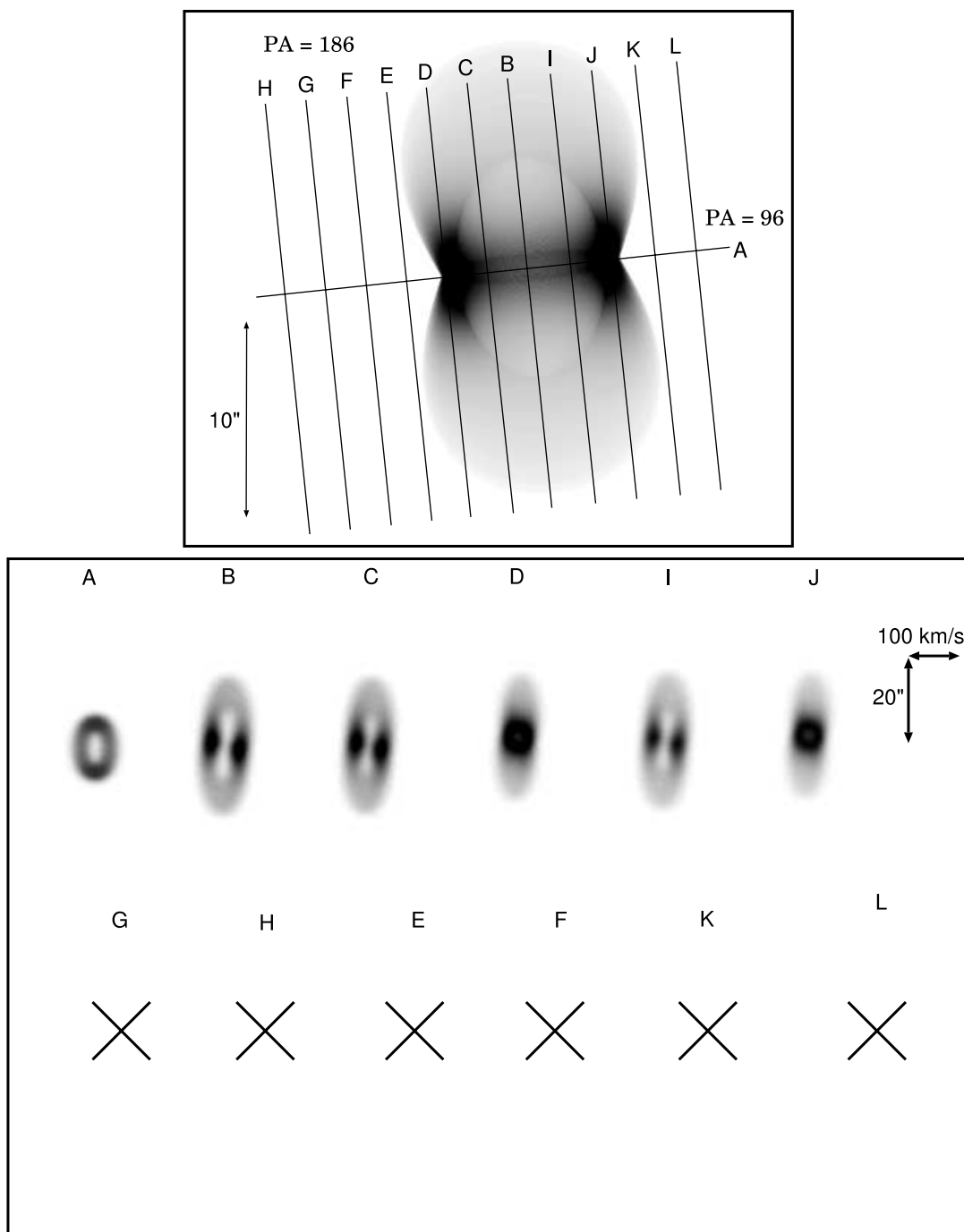


FIG. 54.—NGC 7026 [O III] model image and spectra.

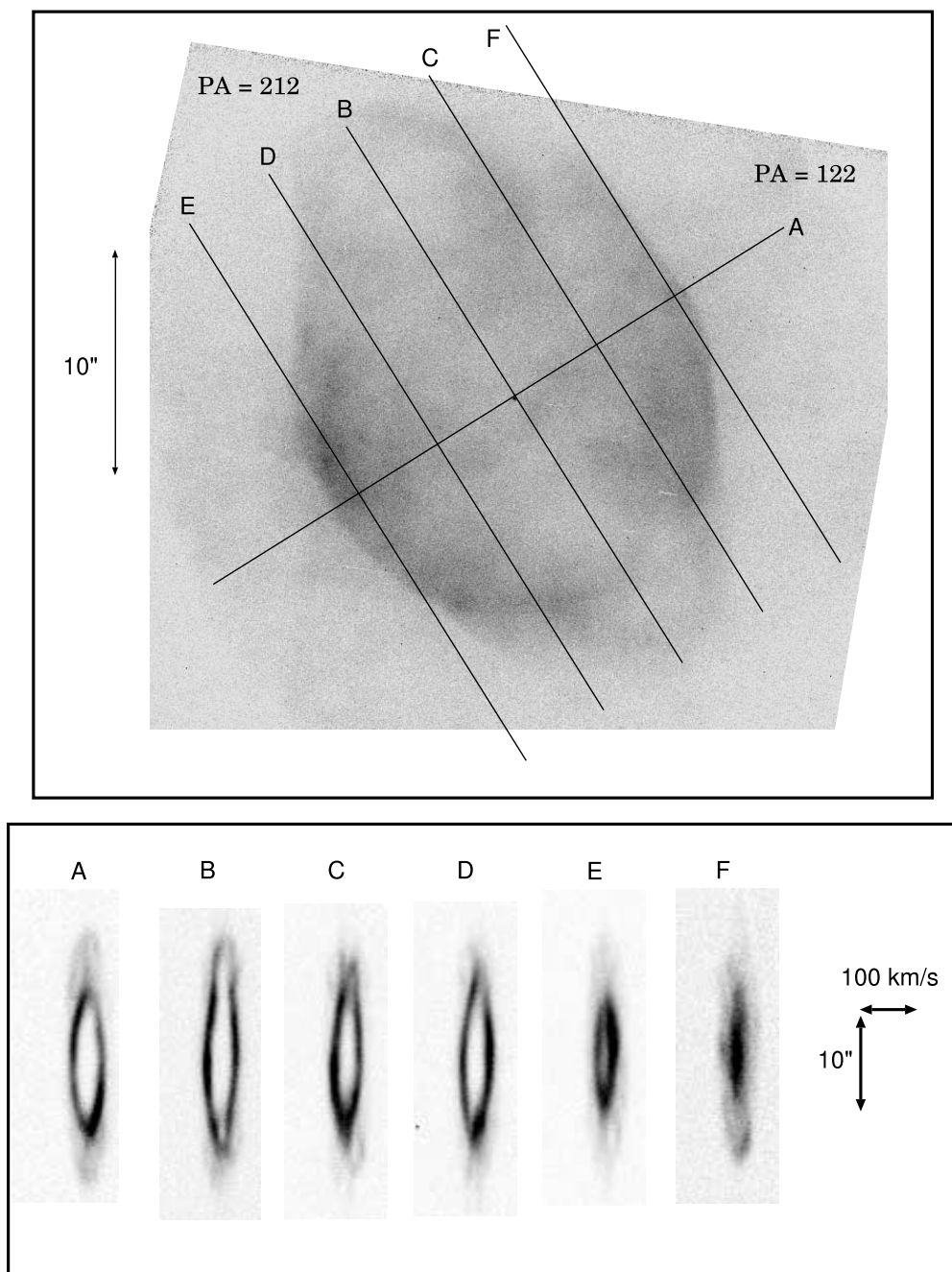


FIG. 55.—NGC 7354 [O III] images from *HST* and spectra from KPNO 1999.

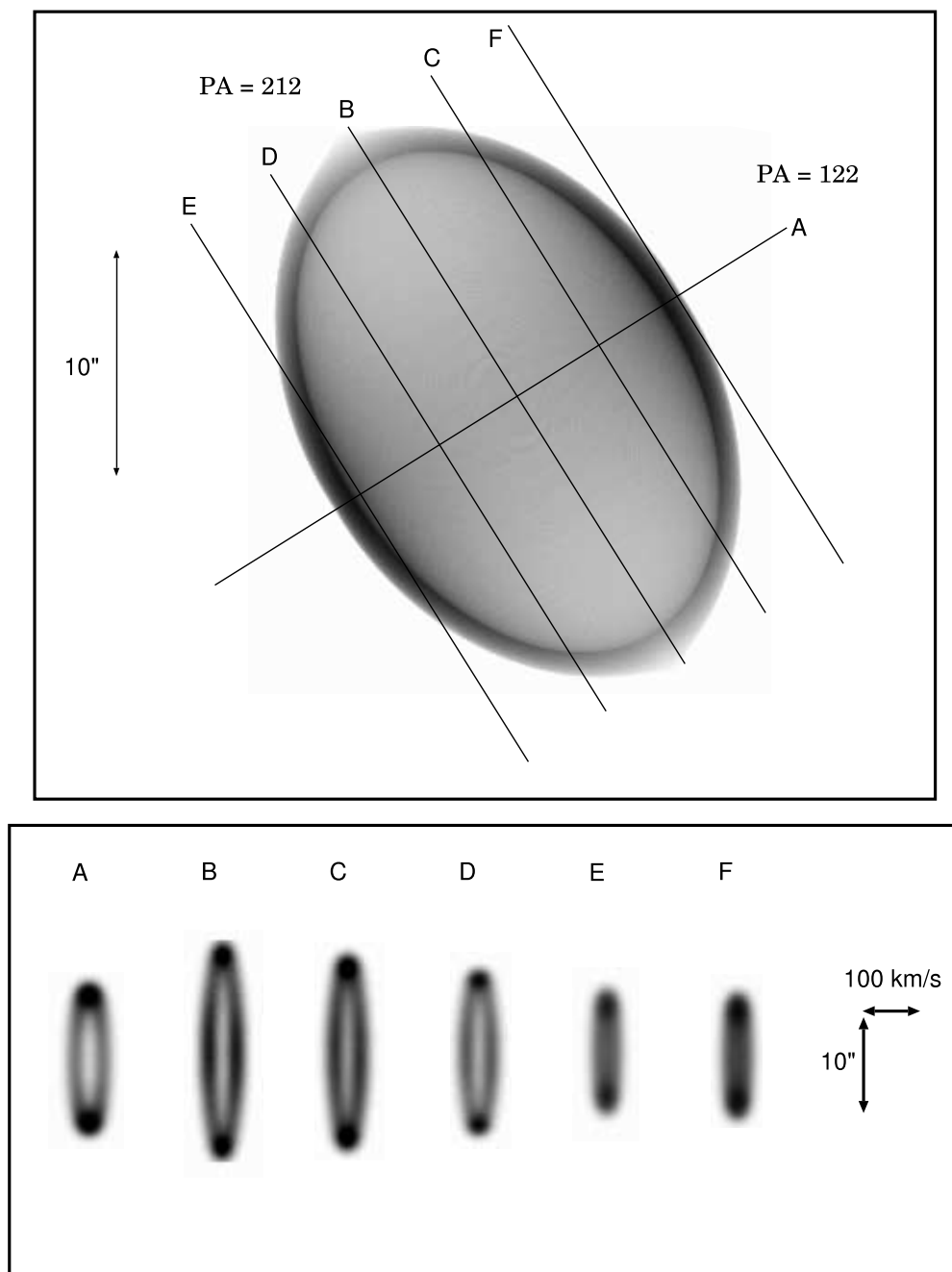


FIG. 56.—NGC 7354 [O III] model image and spectra.

TABLE 3
TABULAR INDEX OF MODEL FITS TO SPECTROSCOPY AND IMAGING OBSERVATIONS

PN	Species	Data Figure	Model Figure	α	β	A_R	I_0	i (deg)	θ' (deg)	v_0 (km s ⁻¹)
BD +30 -3639	[N II]	1	2	0.40	0.15	0.45	12.50	28.6	96.7	11.0
	[O III]	3	4	0.40	0.15	0.40	12.50	28.6	96.7	9.0
	H α	ZK	ZK	1.00	0.90	0.60	...	30.0
IC 2448 (core)	[O III]	5	6a	0.50	0.85	0.85	5.00	85.9	135.0	12.0
IC 2448 (halo)	[O III]	5	6b	0.50	0.85	0.84	4.00	85.9	135.0	22.0
IC 2448	H α	ZK	ZK	1.00	0.90	0.67	...	30.0
IC 3568	[N II]	7	8	1.00	0.85	1.00	3.00	90.0	0.0	14.0
IC 3568 (core)	[O III]	9	10a	1.00	0.85	1.00	3.00	90.0	0.0	12.0
IC 3568 (halo)	[O III]	9	10b	1.00	0.00	0.98	3.00	90.0	0.0	21.4
IC 3568	H α	ZK	ZK	1.00	0.50	1.00	...	30.0
IC 418	[N II]	11	12	0.30	0.30	0.95	10.00	57.3	156.9	13.0
	[O III]	13	14	0.30	0.30	0.82	7.50	57.3	156.9	10.0
	H α	ZK	ZK	1.00	0.50	0.83	...	30.0
IC 4663	[N II]	15	16	2.00	0.50	0.62	5.00	97.4	83.2	30.0
	H α	ZK	ZK	1.00	0.30	0.75	...	32.0
NGC 3132	[N II]	17	18	0.60	0.50	0.58	5.00	122.6	150.0	33.0
	[O III]	19	20	0.60	0.50	0.58	7.00	122.6	150.0	14.0
	H α	ZK	ZK	1.00	0.80	0.71	...	70.0
NGC 5882	[N II]	21	22	0.75	0.50	0.58	4.00	75.7	0.0	26.0
	[O III]	23	24	0.75	0.50	0.58	3.50	75.7	0.0	24.0
NGC 5979	[O III]	25	26	0.75	0.70	0.65	2.50	57.3	152.2	18.0
NGC 6565	[N II]	27	28	1.00	0.40	0.36	3.25	166.2	0.0	17.5
	[O III]	29	30	1.00	0.40	0.36	4.75	166.2	0.0	15.0
	H α	ZK	ZK	1.00	0.90	0.67	...	40.0
NGC 6578	[N II]	31	32	1.00	0.50	0.56	2.75	157.0	123.0	16.0
	[O III]	33	34	1.00	0.50	0.56	2.75	157.0	133.0	15.0
NGC 6741	[N II]	35	36	1.50	0.50	0.54	5.00	120.3	104.0	26.0
	[O III]	37	38	1.50	0.50	0.54	6.00	120.3	104.0	20.0
NGC 6818	[N II]	39	40	1.50	0.70	0.76	2.50	65.9	13.0	30.0
NGC 6826 (core)	[N II]	41	42a	0.75	0.50	0.72	5.00	118.0	120.0	10.0
NGC 6826 (halo)	[N II]	41	42b	0.75	0.50	0.79	3.50	118.0	120.0	22.0
NGC 6884	[O III]	43	44	0.50	0.50	0.62	4.50	117.5	20.0	15.0
NGC 6886	[N II]	45	46	0.30	0.50	0.34	12.00	90.0	130.0	17.5
	[O III]	47	48	0.30	0.50	0.34	12.00	90.0	130.0	13.0
NGC 6891	[O III]	49	50	1.00	0.35	0.66	3.00	120.3	134.0	6.0
NGC 7026	[N II]	51	52	3.00	0.17	0.67	6.00	99.7	6.0	27.5
	[O III]	53	54	3.00	0.17	0.67	6.00	99.7	6.0	24.0
NGC 7354	[O III]	55	56	0.50	0.40	0.66	0.75	91.7	32.0	23.0
	H α	ZK	ZK	1.00	0.20	0.94	...	20.0

NOTES. — The columns represent PN name, species, the number of the figure containing the data and the model fit, respectively (ZK refers to the fit obtained by Zhang & Kwok 1998), α (latitudinal density), β (polar to equatorial density ratio), A_R (axial ratio), I_0 (ionization parameter), i (inclination angle of major axis), θ' (position angle of major axis on sky), and v_0 (equatorial expansion velocity). In all cases, the parameter γ (exponent of radial density power law within the rim) is set to 0.

lengths of the nebular major and minor axes. Because the observed nebular geometry is a strong function of inclination angle, the incorporation of velocity data into a model significantly constrains several parameters, including the axial ratio. Of the nine PNe that we have in common with the analysis performed by Zhang & Kwok (1998), seven had major axis lengths that disagree with our results by more than the 1σ uncertainty (10%). Of the eight nonspherical PNe (IC 3568 is spherical, and therefore its inclination value is irrelevant) seven have inclination angles that exhibit disagreement by more than 1σ (20°). And only four of these eight PNe have axial ratios that are in agreement within 1σ (0.15). These results illustrate the importance of using the velocity data to determine accurate nebular parameters and will have important implications in deriving direct expansion distances to these objects.

Although the quality of our model results is generally a good match to the data, some of the kinematic data show line splittings that the model cannot reproduce. For example, consider Fig-

ures 3 and 4. The data for the “A” slit position in Figure 3 clearly shows the [O III] emission at two discrete velocities, as if a receding and an approaching wall of gas were present. However, the kinematic model along this slit position in Figure 4 shows the line being split in the spatial dimension (i.e., the emission peaks occur at discrete positions). We were unable to remove this effect despite considering a variety of model parameters, and we conclude that the discrepancy is due to a deficiency in the model, perhaps in the way that the gas distribution within the thin nebular shell is treated. The discrepancy between the model and data also appears to be present in some of the [O III] images/spectra but surprisingly is not common in [N II] data sets. This may be a clue to eventually tracking down the source of the disagreement.

4. SUMMARY

In this compilation, we present a catalog of images from the WFPC2 on board *HST*, and long-slit spectra at various positions across a sample of PNe in the light of [N II] and [O III]. Many/most

of the PNe in this compilation are well represented by ellipsoidal geometries. For these targets, we fit models based on the PES model by Aaquist & Kwok (1996) and Zhang & Kwok (1998), and modified to predict the nebular kinematics, as well as spatial morphologies. A comparison between our best-fit parameters and the above-mentioned studies shows differences, mainly resulting from inclusion of the kinematic modeling and resulting parameter constraints that are not provided by the image data alone. The inclination angle and axial ratio of the nebula are strongly affected by inclusion of kinematic data, and most of our estimates are in complete disagreement with estimates based only on image data. The inclination angle of the nebular major axis relative to the line of sight is of special interest to us, since our ultimate goal is to infer expansion distances to these PNe. In addition, the substantially increased spatial resolution offered by the *Hubble Space Telescope* as compared to ground-based observations allows us to completely resolve the nebular shells. Not surprisingly, this has a major impact on estimates of the nebular shell thickness. The precision of the *HST* images and the addition of kinematic data result in better estimates of nebular paramet-

ers, which will enable us to determine accurate distances to the selected PNe.

Support for this work was provided by NASA through grants GO 7501, GO 8390, and GO 8773 from the Space Telescope Science Institute, which is operated by AURA, Inc., under NASA contract NAS 5-26555. A. H. would like to thank Tracy Klayton and Steven Papelian for their assistance with the KPNO 1999 and KPNO 2000 observations. In addition, we acknowledge the excellent observational help and technical assistance from the operations staff at KPNO and CTIO. Y. T. was supported in part by NAIC, which is operated by Cornell University for the National Science Foundation. K. H. K. and K. A. H. were supported in part by NASA Ames Directors Discretionary Fund DDF 274-51-02-51.

IRAF is distributed by the National Optical Astronomy Observatory, which is operated by the Association of Universities for Research in Astronomy, Inc., under cooperative agreement with the National Science Foundation.

REFERENCES

- Aaquist, O. B., & Kwok, S. 1996, *ApJ*, 462, 813
 Fruchter, A. S., & Hook, R. N. 2002, *PASP*, 114, 144
 Hajian, A. R., Terzian, Y., & Bignell, C. 1993, *AJ*, 106, 1965
 Harris, H. C., Dahn, C. C., Monet, D. G., & Pier, J. R. 1997, in *IAU Symp. 180, Planetary Nebulae*, ed. H. J. Habing & H. J. G. L. M. Lamers (Dordrecht: Kluwer), 40
 Holtzman, J. A., Burrows, C. J., Casertano, S., Hester, J. J., Trauger, J. T., Watson, A. M., & Worthy, G. 1995, *PASP*, 107, 1065
 Masson, C. R. 1986, *ApJ*, 302, L27
 ———. 1989a, *ApJ*, 336, 294
 ———. 1989b, *ApJ*, 346, 243
 Palen, S., Balick, B., Hajian, A. R., Terzian, Y., Bond, H., & Panagia, N. 2002, *AJ*, 123, 2666
 Reed, D. S., Balick, B., Hajian, A. R., Klayton, T. L., Giovanardi, S., Casertano, S., Panagia, N., & Terzian, Y. 1999, *AJ*, 118, 2430
 Zhang, C. Y., & Kwok, S. 1998, *ApJS*, 117, 341